2023-12

NUMERICAL SIMULATION OF A UAV WING AND SEVERAL MODIFICATIONS TO IMPROVE RANGE AND ENDURANCE

Jarillo Lopez, Ruben

Monterey, CA; Naval Postgraduate School

NAVAL POSTGRADUATE SCHOOL

MONTEREY, CALIFORNIA

THESIS

NUMERICAL SIMULATION OF A UAV WING AND SEVERAL MODIFICATIONS TO IMPROVE RANGE AND ENDURANCE

by

Ruben Jarillo Lopez

December 2023

Thesis Advisor: Kevin D. Jones
Co-Advisor: Garth V. Hobson

THIS PAGE INTENTIONALLY LEFT BLANK

REPORT DOCUMENTATION PAGE	*Form Approved OMB No. 0704-0188*

Public reporting burden for this collection of information is estimated to average 1 hour per response, including the time for reviewing instruction, searching existing data sources, gathering and maintaining the data needed, and completing and reviewing the collection of information. Send comments regarding this burden estimate or any other aspect of this collection of information, including suggestions for reducing this burden, to Washington headquarters Services, Directorate for Information Operations and Reports, 1215 Jefferson Davis Highway, Suite 1204, Arlington, VA 22202-4302, and to the Office of Management and Budget, Paperwork Reduction Project (0704-0188) Washington, DC, 20503.

1. AGENCY USE ONLY *(Leave blank)*	**2. REPORT DATE** December 2023	**3. REPORT TYPE AND DATES COVERED** Master's thesis

4. TITLE AND SUBTITLE
NUMERICAL SIMULATION OF A UAV WING AND SEVERAL MODIFICATIONS TO IMPROVE RANGE AND ENDURANCE

5. FUNDING NUMBERS

6. AUTHOR(S) Ruben Jarillo Lopez

7. PERFORMING ORGANIZATION NAME(S) AND ADDRESS(ES)
Naval Postgraduate School
Monterey, CA 93943-5000

8. PERFORMING ORGANIZATION REPORT NUMBER

9. SPONSORING / MONITORING AGENCY NAME(S) AND ADDRESS(ES)
N/A

10. SPONSORING / MONITORING AGENCY REPORT NUMBER

11. SUPPLEMENTARY NOTES The views expressed in this thesis are those of the author and do not reflect the official policy or position of the Department of Defense or the U.S. Government.

12a. DISTRIBUTION / AVAILABILITY STATEMENT
Approved for public release. Distribution is unlimited.

12b. DISTRIBUTION CODE
A

13. ABSTRACT (maximum 200 words)

This thesis presents numerical simulations aimed at improving the aerodynamic performance of an unmanned aerial vehicle (UAV) wing through minor modifications. On most aircraft, the bulk of the lift and a large portion of the drag are produced by the wing; therefore, optimization of the wing is likely to have the most significant impact on aircraft performance, including critical parameters like range and endurance. When minor changes are required, there are prominent options to explore for improving the wing's aerodynamic efficiency. Three different configurations were analyzed; wing extension, raked wingtip, and blended winglet, to find which affects in a more positive way the performance of the UAV wing. Taking advantage of the short processing time delivered for low-fidelity numerical tools like Flow5, the exploration of the main parameters for the three configurations were explored and optimized to reach the best lift to drag ratio (L/D). Finally, the optimized configurations were analyzed using Ansys-CFX software to capture the viscous effects and boundary layer behavior more accurately, which are known limitations of the low-fidelity tools. The study found that incorporating raked wingtips into the UAV wing design is the most effective way to improve the aircraft's range and endurance. This modification only slightly increases the wing bending moment and has practically no impact on the pitching moment.

14. SUBJECT TERMS UAV, unmanned aerial vehicle, aerodynamics analysis, winglets design, vortex panel methods, computational fluid dynamics	**15. NUMBER OF PAGES** 103
	16. PRICE CODE

17. SECURITY CLASSIFICATION OF REPORT	**18. SECURITY CLASSIFICATION OF THIS PAGE**	**19. SECURITY CLASSIFICATION OF ABSTRACT**	**20. LIMITATION OF ABSTRACT**
Unclassified	Unclassified	Unclassified	UU

NSN 7540-01-280-5500

Standard Form 298 (Rev. 2-89)
Prescribed by ANSI Std. 239-18

THIS PAGE INTENTIONALLY LEFT BLANK

Approved for public release. Distribution is unlimited.

NUMERICAL SIMULATION OF A UAV WING AND SEVERAL MODIFICATIONS TO IMPROVE RANGE AND ENDURANCE

Ruben Jarillo Lopez
Capitan de Corbeta, Mexican Navy
Bachelor of Science in Naval Mechanical Engineering,
School of Engineering of the Mexican Navy, 2009

Submitted in partial fulfillment of the
requirements for the degree of

MASTER OF SCIENCE IN AEROSPACE ENGINEERING

from the

NAVAL POSTGRADUATE SCHOOL
December 2023

Approved by: Kevin D. Jones
Advisor

Garth V. Hobson
Co-Advisor

Brian S. Bingham
Chair, Department of Mechanical and Aerospace Engineering

THIS PAGE INTENTIONALLY LEFT BLANK

ABSTRACT

This thesis presents numerical simulations aimed at improving the aerodynamic performance of an unmanned aerial vehicle (UAV) wing through minor modifications. On most aircraft, the bulk of the lift and a large portion of the drag are produced by the wing; therefore, optimization of the wing is likely to have the most significant impact on aircraft performance, including critical parameters like range and endurance. When minor changes are required, there are prominent options to explore for improving the wing's aerodynamic efficiency. Three different configurations were analyzed; wing extension, raked wingtip, and blended winglet, to find which affects in a more positive way the performance of the UAV wing. Taking advantage of the short processing time delivered for low-fidelity numerical tools like Flow5, the exploration of the main parameters for the three configurations were explored and optimized to reach the best lift to drag ratio (L/D). Finally, the optimized configurations were analyzed using Ansys-CFX software to capture the viscous effects and boundary layer behavior more accurately, which are known limitations of the low-fidelity tools. The study found that incorporating raked wingtips into the UAV wing design is the most effective way to improve the aircraft's range and endurance. This modification only slightly increases the wing bending moment and has practically no impact on the pitching moment.

THIS PAGE INTENTIONALLY LEFT BLANK

TABLE OF CONTENTS

LIST OF FIGURES

LIST OF TABLES

THIS PAGE INTENTIONALLY LEFT BLANK

LIST OF ACRONYMS AND ABBREVIATIONS

AoA	angle of attack
AR	aspect ratio
β	cant angle
b	wingspan
Cbm	bending moment coefficient
Cd	drag coefficient
CFD	computational fluid dynamics
Cl	lift coefficient
Cm	pitching moment coefficient about ¼ of root chord
E	endurance
i	internal energy
L/D	lift-to-drag ratio
LLT	Lift Line Theory
MAC	mean aerodynamic chord
MOPSO	multi-objective particle smarm optimization
P_R	power required
p	pressure
PSO	particle swarm optimization
q_∞	freestream dynamic pressure
R	range
RANS	Reynolds averaged Navier Stokes
S	wing reference area
SST	Shear Stress Transport
S_{Mx}	x-momentum source term
S_{My}	y-momentum source term
S_{Mz}	z-momentum source term

S_i	internal energy source term
T_R	thrust required
UAV	unmanned aerial vehicle
u	x-velocity component
v	y-velocity component
w	z-velocity component
VLM	Vortex Lattice method
V_∞	freestream velocity
Γ	strength of the vortex filament flow field
ρ	density
μ	dynamic viscosity
Φ	dissipation function

I. INTRODUCTION

This study is focused on improving the aerodynamic performance of a fixed-wing, low-speed unmanned aerial vehicle (UAV) developed by the Mexican Navy. This UAV was initially designed with the ability of vertical takeoff and landing (VTOL). While the VTOL capability is convenient in different operational scenarios, this functionality increases the gross weight by about 25%. Since range and endurance are always desirable characteristics in UAV operations, there is a requirement to modify the aircraft for a conventional runway takeoff and landing, giving up the VTOL capability to improve the airplane's aerodynamic performance. The intention of this study is to implement minor modifications to the wing that can enhance the aerodynamic efficiency. To minimize the cost and complexity of the changes, they will be limited to minor modifications to the wing that can easily be implemented on the current design. An in-depth analysis of the existing wing configuration determines if a complete wing redesign is required or if the objective can be accomplished with minor modifications like wing extensions or wingtip devices.

On most aircraft, the bulk of the lift and a large portion of the drag are produced by the wing; therefore, optimization of the wing is likely to have the most significant impact on aircraft performance, including critical parameters like range and endurance. The lift-over-drag (L/D) ratio is known as the wing's aerodynamic efficiency. There are some prominent options to consider when minor changes are required to enhance wing aerodynamics. The first option is to add wing extensions looking for a more elliptical lift distribution, consequently reducing the induced drag and hopefully getting a better L/D ratio. However, parasitic drag also increases in some amount while adding more wetted area.

Another option is to explore wingtip devices like raked wingtip, blended winglet, and tip fence, among others, to try to reduce the induced drag while increasing the AR at the same time. The exploration of a more efficient airfoil for wingtip devices also contributes to the improvement of the final aerodynamic efficiency of the wing.

II. DRAG BREAKDOWN

Over the last century, aircraft design has primarily focused on reducing drag [1]. Drag prediction is not a simple task because many factors are difficult to characterize and measure correctly. When it comes to full-scale aircraft, the errors in predicting drag can range from 10–20%[2]. The most common drag divisions are parasite drag and induced drag; the first is independent of lift, and the second is known as drag due to lift. Also, drag can be classified depending on the natural forces acting on the body: pressure drag and friction drag. Finally, drag can also be broken down by the sources that generate it: vortical flow, viscosity of air, and shock waves. The drag breakdown is shown in Figure 1.

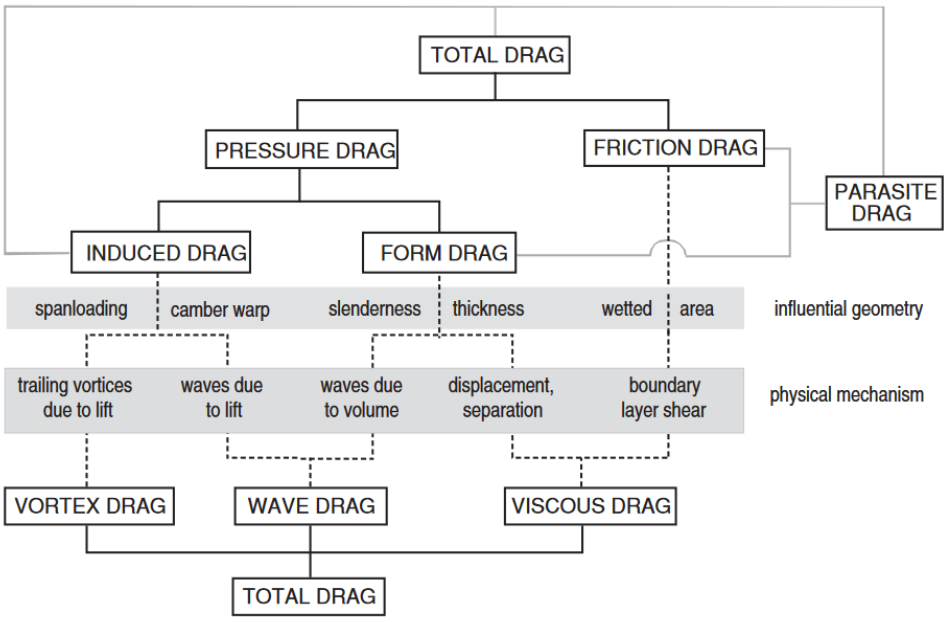

Figure 1. Drag decomposition of a closed lifting body. Source: [3].

To effectively reduce drag, it is essential first to identify its sources and quantify the magnitude of each type of drag. The parasite drag (both friction and form drag) cannot be minimized without significant changes to the wing, and since the UAV is a

low-velocity airplane, wave drag is not a problem to consider. As a result, the only type of drag that can be reduced is the induced drag, specifically the vortex drag.

McLean [4] defines the drag part derived from the global effects of lift as induced drag. It is a type of pressure drag that occurs due to the creation of lift by a finite wing. The movement of air over the wing generates lift, which is accompanied by a force called lift-induced drag. The wing experiences downwash from the tip vortices, changing the pressure distribution over the wing reducing the lift.

For a typical transport aircraft at cruise conditions, the induced drag constitutes about 40% of the total drag [1]. At lower velocities, this effect is even more critical; as can be seen in Figure 2, the vortex wake is generated by the pressure difference between the upper and lower faces of the wing. At the wing tip, the difference in pressure between the high-pressure area below the wing and the low-pressure area on top is more noticeable.

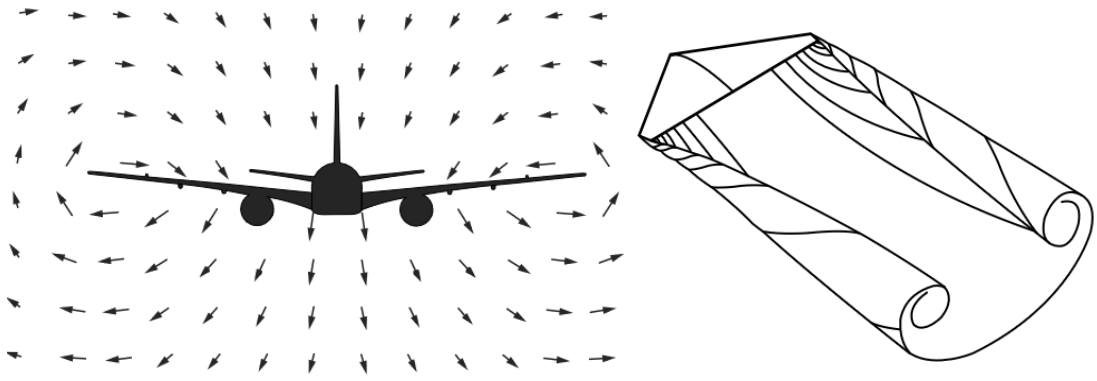

Figure 2. Velocity vectors developed in a crossflow plane (left) and vortex wake formed behind a lifting wing (right). Adapted from [4].

The goal is to reduce the induced drag; therefore, the first step is to measure it. The induced drag for a planar wing is given by Equation 1 [5],

$$D_i = \frac{L^2}{\frac{1}{2}\rho V^2 \pi e b^2}, \tag{1}$$

where L is the lift force, ρ is the air density, V is the freestream velocity, e is the span efficiency factor, and b is the wingspan. The Oswald efficiency factor (e), which represents the pressure distribution along the wingspan, is typically between 0.7 and 0.8, considering the elliptical distribution to have a value of 1. Raymer [6] proposes Equation 2 to compute this parameter for a straight-wing aircraft:

$$e = 1.78\left(1 - 0.045 * AR^{0.68}\right) - 0.64, \tag{2}$$

where AR is the wing aspect ratio and can be computed with Equation 3,

$$AR = \frac{b^2}{S}. \tag{3}$$

The relation of drag and lift coefficients with the induced drag are established in Equation 4:

$$C_{D_i} = \frac{D_i}{\frac{1}{2}\rho V^2 S} = \frac{C_L^2}{\pi ARe}, \tag{4}$$

where S is the wing planform area and C_L is the lift coefficient, which is computed with Equation 5,

$$C_L = \frac{L}{\frac{1}{2}\rho V^2 S}. \tag{5}$$

According to Equation 1, induced drag is inversely proportional to the square of the freestream velocity. As such, higher velocities result in lower induced drag. However, the total drag consists not only of induced drag but also of parasite drag, which increases with velocity squared. Therefore, a point exists where the minimum L/D ratio occurs. Figure 3 illustrates the relationship between these two types of drag and approximates the optimal intermediate velocity for flight. It is essential to identify the optimal velocity of operation, as this is the ideal velocity for cruise conditions to achieve the maximum endurance for the UAV.

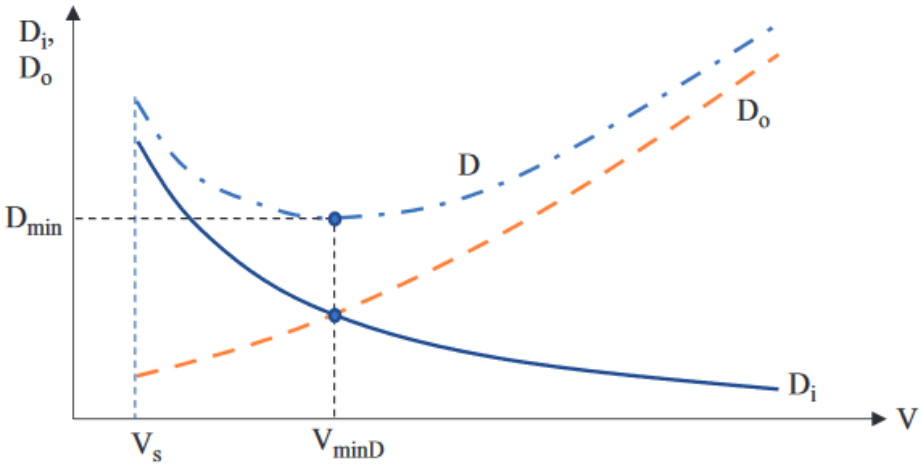

Figure 3. Variations of drag (D), zero-lift drag (D_0), and induced drag (D_i). Source: [7].

THIS PAGE INTENTIONALLY LEFT BLANK

III. INDUCED DRAG REDUCTION

Drag reduction techniques have been studied for a long time and are still an essential issue in the aerodynamic field. Various aerodynamic devices, particularly wingtip devices, have been developed and implemented to reduce induced drag by minimizing the formation and effects of wingtip vortices. These devices enhance the wing's aerodynamic efficiency and reduce the aircraft's overall drag. Some of the concepts and devices implemented to explore drag reduction are presented in this section.

A. ASPECT RATIO

As shown in previous equations, it is evident that induced drag decreases as the aspect ratio increases. Thus, increasing the wing-aspect ratio by extending the wingspan is a logical way to reduce this drag type. According to Kroo [8], achieving up to a 17% reduction in vortex drag is possible by increasing the wingspan by 10% while maintaining a fixed speed and lift. However, this solution has some drawbacks; the most significant is the increase in bending moment.

To support more prominent bending moments derived from high aspect ratio wings, the structure needs to be stronger, leading to an increase in the final weight of the aircraft. Therefore, there are mechanical limitations to consider when attempting to reduce the induced drag by only increasing the aspect ratio. Furthermore, Bertin and Cummings [9] state that for small aircraft (such as small UAVs), the dominant parameter in drag production shifts from the aspect ratio to skin friction. Similarly, Drela et al. state that there exists an aircraft size for each aspect ratio that can maximize the range: "This is because, as the aspect ratio increases, the wing is proportionately heavier for a large vehicle than for a smaller vehicle, while at a small size, drag is more important so that the increasing friction drag with aspect ratio offsets the reduction in induced drag" [10, p. 4]. The same analogy is valid for wing loading. Hence, an optimal combination of aspect ratio and wing loading exists for each aircraft size that maximizes the range. Figure 4 illustrates this optimum relationship.

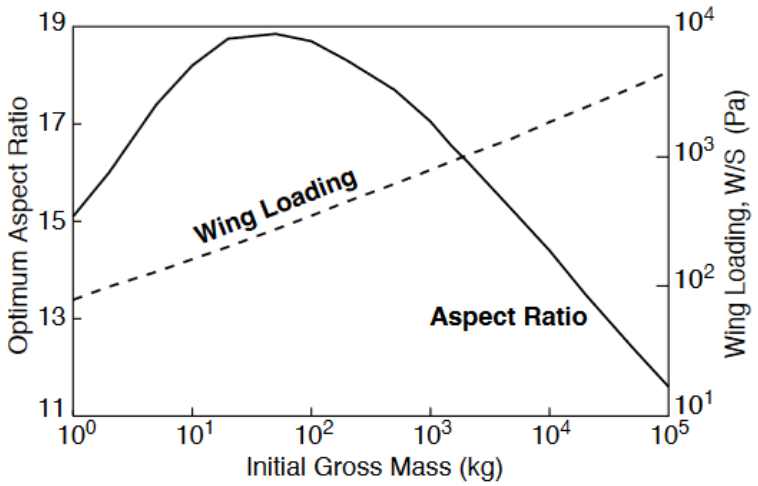

Figure 4. Wing loading and aspect ratio optimized for range at each aircraft size. Source: [10].

B. NON-PLANAR WINGS

Non-planar wing concepts are an excellent opportunity to look for drag reduction and even improve other characteristics of the aircraft, like high lift or better control and stability. Kroo [8] studied some non-planar wing concepts and defined the span efficiency as the ratio of a planar wing's induced drag over the non-planar system's induced drag with the same span and lift. He pointed out that about 30% drag reduction can be achieved when adding vertical extents to the wingtip with a height-to-span ratio of 0.2 for a fixed-span wing. The span efficiency comparison for some non-planar wing configurations is illustrated in Figure 5, showing that the box is the most efficient system. This type of configuration has been studied by Mamla and Galinski [11], ending with the joined-wing configuration, which was found to result in some structural and control difficulties. Less complicated configurations with similar results are more attractive for reducing the induced drag of a low-velocity UAV.

The vertical extension at the tip is what leads to the improvement of span efficiency, according to Figure 5, where the wingtip devices, the C-shape and winglets, appear promising. However, implementing the C-shape on small aircraft such as UAVs can be more challenging due to its complexity, increased friction drag, and possible flutter derived from the torsional inertia. Therefore, wingtip devices or winglets seem to

be the better options for reducing induced drag, as they are nearly as efficient as the C-shape but do not require significant structural challenges and modifications.

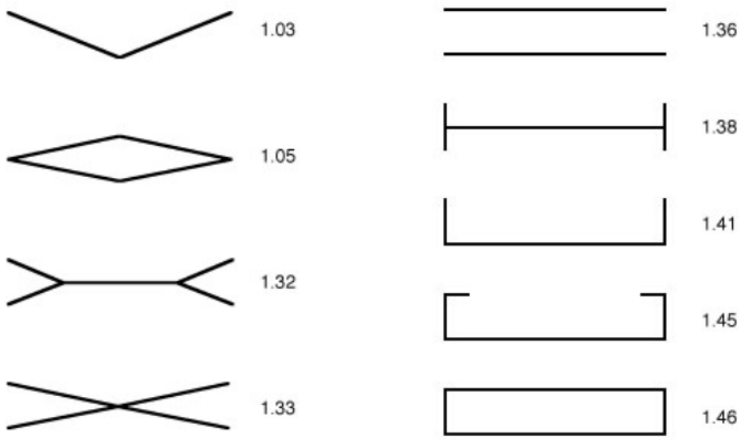

Figure 5. Span efficiency for different optimally loaded nonplanar systems (h/b=0.2). Source: [8].

There are different types of wingtip devices; the variety of designs is driven by the type of aircraft and mission performed. Some types of winglets and wingtip devices are presented in Figure 6. One of the first studies to reduce the vortex drag was developed by Whitcomb [12] in 1976. He introduced the term *winglet* to describe a high-aspect ratio endplate. His results showed that winglets were more than twice as effective as a wingtip extension at improving L/D at a specific Mach number of 0.78.

1. Winglets

Several research investigations have examined the variations among winglet designs to identify the most suitable shape that fulfills the necessary flight requirements. Maughmer [13] states the following design variables to define the geometry of the winglet: airfoil, chord distribution, height, twist, sweep, cant angle, and toe angle. These parameters are shown in Figure 7.

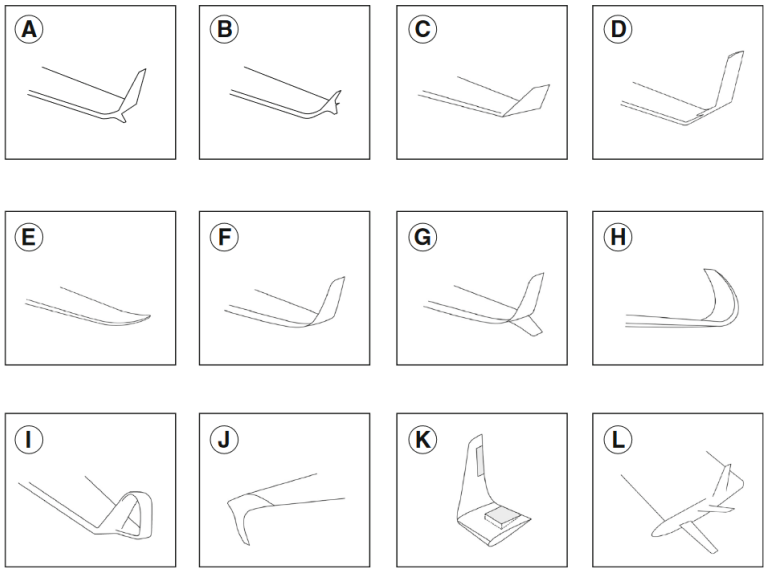

Figure 6. Different types of winglets and wingtip devices. Source: [14]. A) Whitcomb winglet. B) Tip fence. C) Canted winglet. D) Vortex diffuser. E) Raked winglet. F) Blended winglet. G) Blended split winglet. H) Sharklet. I) Spiroid winglet. J) Downward canted winglet. K) Active winglets. L) Tip sails.

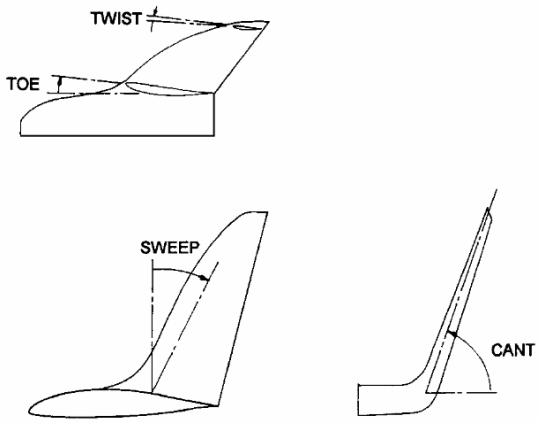

Figure 7. Design variables used to define winglet geometry. Source: [13].

Makgantai et al. [15] conducted a study using Aeolus Aero Sketch Pad ASP, which is based on a three-dimensional panel method Kernel to analyze the aerodynamic performance, L/D ratio, and endurance of three different wingtip devices: blended winglets, drooped wingtip, and spiroid winglets. Their results showed that blended winglets with a cant angle (β) of 60 degrees were the most effective in reducing drag.

These findings were consistent with experimental studies conducted by Belferhat et al. [16], who found that winglets can significantly impact airplane performance. Belferhat et al. conducted experimental tests in a wind tunnel to determine the optimal winglet shape, focusing on varying the cant angle β under different velocity conditions. The tests were conducted at different Reynolds numbers (2.35E5, 2.84E5, and 3.03E5) and incidence angles from 0 to 20 degrees. The results are shown in Figure 8, where the cant angle β=55 degrees produced the maximum L/D ratio, at least for the physical properties tested in the experiment. These studies demonstrate the reliability of computational tools like Aeolus Aero Sketch Pad ASP, which are in agreement with experimental methods.

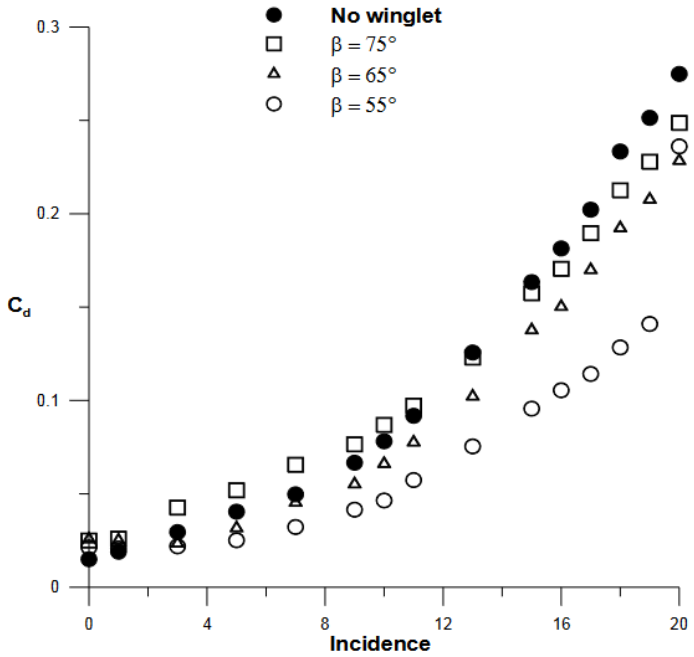

Figure 8. Effect of cant angle variations on winglets performance. Source: [16].

2. Raked Wingtips

Prieto et al. [17] developed a study on a drone with VTOL capability, looking for aerodynamic optimization by implementing wingtip devices and winglets. They utilized two methods: the open-source Xflr5 software, which uses the Vortex Lattice method (VLM) approach, and the OpenFoam software, a computational fluid dynamics (CFD)

tool that solves the Reynolds Averaged Navier Stokes (RANS) equations. The results from both sources were compared, and while Xflr5 overestimated lift and viscous drag while underestimating induced and total drag, the trends observed were consistent across both tools. Since VLM computations are significantly faster and less computationally intensive than CFD simulations are, Xflr5 is a viable choice during the initial design stages. The graphical results are presented in Figure 9. As seen in that plot, the Raked wingtips perform even better than winglets. According to Prieto et al., winglets are most effective in reducing induced drag under certain conditions, particularly during high angles of attack, such as climbing. However, during most of the flight time in cruise conditions with small angles of attack, Raked wingtips demonstrate better performance. It is important to note that using Raked wingtips comes with the drawback of increased bending moment. In the case of UAVs, this impact is frequently not severe, as composite materials used in UAV wing construction typically have a suitable safety factor. If reinforcement is required, it would only result in a minor increase in overall wing weight.

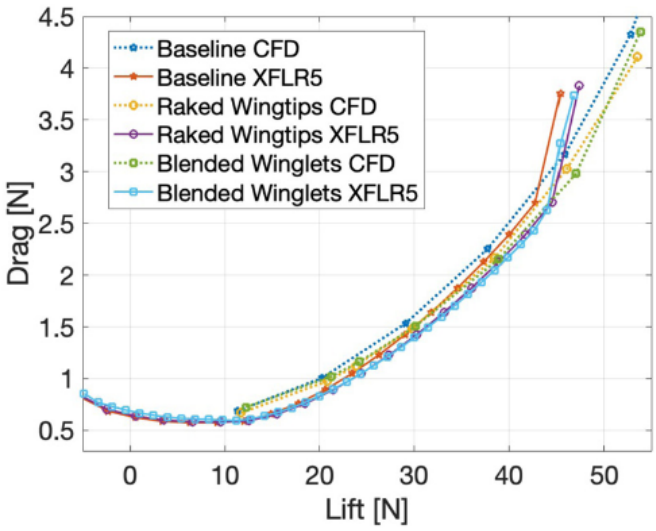

Figure 9. Drag as a lift function for different wingtip devices analyzed with different tools. Source: [17].

IV. METHODS AND TOOLS

Several researchers have conducted studies to design and optimize winglets using tools such as the VLM, computational fluid dynamics (CFD), and experimental tests. Weierman [18] used VLM to analyze the impact of winglets on the aerodynamic properties of UAV wings, focusing on different wing configurations, and they compared the results with experimental data from wind tunnel tests. To compute the aerodynamic load distribution, they used VLM, specifically the open-source Tornado software, which had relatively low computational requirements and could quickly analyze different configurations. The study revealed that while VLM did not produce precise results, it helped predict performance trends. This method is valid during the initial design stage when parametric analysis is necessary to identify prominent configurations. However, more precise tools, such as CFD, that solve the RANS equations are required for a more in-depth analysis, including the ability to capture the behavior of the boundary layer and viscous effects on the surface. This type of analysis demands greater computational power and time consumption to configure and run simulations correctly.

From previous references, it is known that a combination of VLM and CFD is a suitable approach to perform the design and analysis of wingtip devices. Each method has its advantages and disadvantages. To design a suitable winglet for a particular aircraft under specific flight conditions, it is necessary to calculate the flow field for the wing. The VLM is appropriate for calculating the aerodynamic load distribution at velocities where incompressible assumptions are considered, including induced drag [9]. Even though VLM typically underestimates the viscous drag, it can be a very efficient approach to survey an ample parameter space for design exploration.

A. VORTEX LATTICE METHOD

The VLM is a widely used aerodynamic analysis tool for predicting the flow field around wings and lifting surfaces. It has been employed in various aerospace applications, including aircraft design, performance analysis, and optimization. This method is based on the solution of the Laplace's equation and the Biot-Savart law,

$$\mathbf{dw} = \frac{\Gamma}{4\pi} \frac{\mathbf{dl} \times \mathbf{r}}{|\mathbf{r}|^3}, \tag{6}$$

which is widely used for inviscid and incompressible flows [19].

The parameters expressed in Equation 6 are shown graphically in Figure 10. The vortex filament produces a flow field with circulation depending on its strength, denoted by Γ. Let consider a specific part of the filament, represented by **dl**. At an arbitrary point P in space, the radius vector from **dl** to P is denoted as **r**. The segment **dl** induces a velocity at point P.

When multiple vortex filaments are combined with a uniform freestream, it becomes possible to create a flow over a finite wing to characterize its performance.

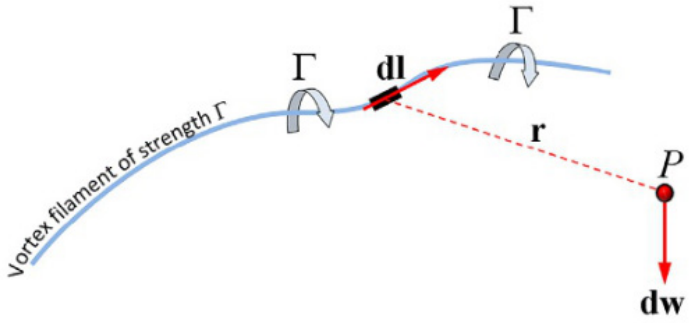

Figure 10. Illustration of the Biot-Savart law for a vortex filament. Source: [19].

Hermann von Helmholtz was the first to apply the concept of vortex filaments to analyze inviscid, incompressible flow. He established the following key principles, known as Helmholtz's vortex theorems:

- The strength of a vortex filament is constant along its length.
- A vortex filament cannot end in a fluid; it must extend to the boundaries of the fluid (which can be $\pm\infty$) or form a closed path. [19, p. 435]

The first practical theory for predicting the aerodynamic characteristics of finite wings was developed by Ludwig Prandtl. This theory, known as Prandtl's Lifting-Line theory, remains in use today for preliminary calculations of finite wing properties. Prandtl's approach was based on the concept of a bound vortex, a vortex filament of strength Γ that is fixed in a flow. According to the Kutta–Joukowski theorem, this bound vortex experiences a force $L' = \rho_\infty V_\infty \Gamma$. To represent a finite wing with a span b, Prandtl proposed replacing it with a bound vortex extending from $y = -b/2$ to $y = b/2$, as illustrated in Figure 11 [19]. However, per von Helmholtz's theorem, a vortex filament cannot terminate within the fluid. Prandtl's theory suggests that the vortex filament of a wing continues on as two free vortices, creating a horseshoe vortex shape consisting of the bound vortex and the two free vortices. These vortices trail downstream from the wingtips to infinity.

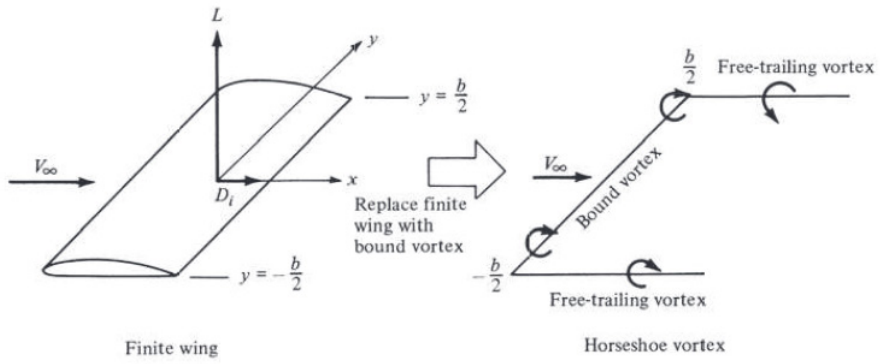

Figure 11. Representation of finite wing with a bound vortex. Source: [19].

The technique of representing a wing by a group of horseshoe vortices was initially introduced in the late 1930s. In 1943, Faulkner gave it the name "Vortex Lattice" [20]. As mentioned in previous paragraphs, the VLM is based on the principle of modeling a lifting surface as a collection of horseshoe-shaped vortex filaments. These filaments represent the vorticity generated by the wing and capture the main flow characteristics. The method involves discretizing the wing into a lattice of panels,

calculating the circulation and induced velocities at each panel, and solving a set of linear equations to determine the aerodynamic forces and moments.

Even though the VLM is not a precise method, it has wide use in different applications, for example, in analyzing and designing aircraft wings and configurations at subsonic speeds. There is a close relationship with wind tunnel data, but this only happens for Mach numbers below 0.8 [20]. It allows for quick and computationally efficient estimation of aerodynamic coefficients, including lift, induced drag, and pitching moment. It has been applied in preliminary design studies, optimization processes, and performance evaluations.

Despite its widespread use, the VLM has certain limitations. It assumes potential flow and neglects viscous effects, making it less suitable for regions with flow separation or near-field flow interactions. The method is most accurate at low-to-moderate angles of attack and subsonic speeds.

1. XFLR5

Xflr5 is an open-source computer program used for analyzing and simulating the aerodynamic properties of airfoils, wings, and complete aircraft. It is based on the Lifting-Line Theory, VLM, and 3-D Panel Method [21]. The software can calculate lift, drag, moments, and other aerodynamic characteristics of configurations. It is designed explicitly for low-speed aerodynamics, making it suitable for applications such as model aircraft, gliders, and small general aviation aircraft. Therefore, it is a convenient option for analyzing UAV aerodynamics.

The software utilizes a user-friendly graphical interface, allowing users to input the airfoil or wing geometry, define the flight conditions, and specify parameters such as Reynolds number and angle of attack. The program then performs a series of calculations based on the VLM, generating predictions of lift, drag, pitching moment, and other performance indicators [22].

Because Xflr5 provides a convenient and accessible tool for aerodynamic analysis and exploration of multiple configurations, this software and Flow5 are used to explore

the initial designs of wingtip devices to evaluate and refine the more prominent configurations that deserve to be analyzed by CFD software. Its simplicity, computational efficiency, and reasonable accuracy make it suitable for conceptual design and initial aerodynamic assessments. However, its limitations must be considered, and it should be used in conjunction with other methods, such as CFD or wind tunnel testing, when possible, to validate the results.

2. FLOW5

The Flow5 software is a potential flow solver that incorporates the fundamental functionalities of Xflr5 while also introducing new features to enhance its user-friendliness, versatility, and precision. This potential flow solver includes the following methodologies:

- a method based on non-linear Lifting-Line Theory, following the approach outlined in the NACA-1269 report [23]
- two VLMs, the first of which involves the use of horseshoe and the second that applies quad ring vortices to simulate the flow of air around the body
- a method derived from the National Aeronautics and Space Administration (NASA) 4023 report [24], which also applies a volume quad panel method
- one based on Galerkin formulations, which also uses two triangular panel methods. Triangular methods are advantageous for describing diverse 3D surfaces. This linear method notably enhances prediction accuracy when dealing high local pressure gradients [25].

To accurately model fluid flow behavior, the impact of viscosity must be considered. Xflr5 and Flow5 provide practical corrections to approximate skin friction, since they are based mainly on Lift Line Theory (LLT), 3D panels methods, and VLM, which are deducted from fluids with inviscid assumptions, which are unable to compute viscous stresses. The only way this software computes the viscous effect is by

extrapolating 2D data [26]. This calculation obviously does not provide precise results for the real viscous effects of the geometry analyzed. Therefore, CFD analysis is necessary to verify the final configurations.

Considering the software's previous advantages and characteristics, I am using the Xflr5 and Flow5 software to explore various configurations of the UAV wing to improve the L/D ratio, and, finally, ANSYS-CFX is used to validate the results.

B. COMPUTATIONAL FLUID DYNAMICS

As a branch of fluid mechanics, CFD focuses on the analysis and numerical simulation of fluid flow and heat transfer using computer algorithms. CFD involves using computational methods and mathematical models to solve the governing equations of fluid dynamics, such as the RANS equations, to predict and visualize fluid flow behavior. CFD has become an essential tool in various industries, including aerospace. It enables the study and optimization of the performance of complex fluid systems without relying solely on expensive and time-consuming experimental testing.

Turbulence modeling involves developing a set of partial differential equations to simulate turbulent flow; the equations are based on approximate versions of the exact Navier-Stokes equations. Generally, it is impossible to fully resolve the full scale of turbulent flow structures in any practical flow. For the RANS equations, the process begins with the Reynolds decomposition, separating the flow variables into mean and fluctuating components. By substituting these variables into the Navier-Stokes equations and subsequently averaging the equations, the Reynolds stress tensor emerges as an unknown term that needs to be modeled to solve the RANS equations [27]. Versteeg and Malalasekera [28] present the governing equations (Equations 7, 8, and 9) in a conservative form, of a 3D time dependent fluid flow for a compressible Newtonian fluid.

The continuity equation is:

$$\frac{\partial \rho}{\partial t} + \operatorname{div}(\rho \mathbf{u}) = 0 \tag{7}$$

The momentum equations are:

$$\begin{aligned}
\frac{\partial(\rho u)}{\partial t} + \operatorname{div}(\rho u \mathbf{u}) &= -\frac{\partial p}{\partial x} + \operatorname{div}(\mu \operatorname{grad} u) + S_{Mx} \\
\frac{\partial(\rho v)}{\partial t} + \operatorname{div}(\rho v \mathbf{u}) &= -\frac{\partial p}{\partial y} + \operatorname{div}(\mu \operatorname{grad} v) + S_{My} \\
\frac{\partial(\rho w)}{\partial t} + \operatorname{div}(\rho m \mathbf{u}) &= -\frac{\partial p}{\partial z} + \operatorname{div}(\mu \operatorname{grad} w) + S_{Mz}
\end{aligned} \tag{8}$$

The energy equation is:

$$\frac{\partial(\rho i)}{\partial t} + \operatorname{div}(\rho i \mathbf{u}) = -p \operatorname{div} \mathbf{u} + \operatorname{div}(k \operatorname{grad} T) + \Phi + S_i \tag{9}$$

The process of performing an accurate CFD calculation is quite extensive and complicated. The precision of results relies on a well-executed process, which often has a steep learning curve. The CFD process typically involves the following steps:

1. Geometry definition: Creating a digital representation of the physical system using computer-aided design (CAD) tools.
2. Mesh generation: Dividing the computational domain into a grid of discrete elements. This discretization enables the representation of fluid flow variables at specific locations within the domain.
3. Governing equations: Formulating and discretizing the governing equations of fluid flow, such as the conservation of mass, momentum, and energy, to obtain a system of algebraic equations.
4. Numerical solution: Solving discretized equations using numerical methods such as finite volume. The objective of these methods is to approximate the fluid flow behavior in each grid element or cell.

5. Boundary conditions: Specifying the conditions at the boundaries of the computational domain, including inflow, outflow, wall conditions, and symmetry conditions. These conditions define the interaction between the fluid and the boundaries.

6. Turbulence modeling: Incorporating turbulence models to capture the effects of turbulent flow behavior. Turbulence models approximate the complex interactions of turbulent eddies within the flow.

7. Solution and analysis: Performing the numerical calculations to obtain the solution for the fluid flow variables, such as velocity, pressure, temperature, and other relevant parameters, and analyzing the results to gain insights into the behavior of the fluid system.

CFD simulations can provide valuable information about flow patterns, pressure distributions, heat transfer rates, and other essential characteristics of fluid systems. CFD is a valuable tool to optimize designs, evaluate performance, and make informed decisions without extensive prototyping and testing. However, it is essential to note that CFD simulations are based on mathematical models and assumptions, and their accuracy depends on the input data quality and the chosen models' validity. Mesh quality plays an essential role in the accuracy of results delivered.

ANSYS-CFX is a well-known CFD commercial software. This software offers advanced capabilities for modeling and simulating fluid flow problems. It provides a user-friendly interface, extensive pre-processing tools for geometry creation and mesh generation, and efficient solvers to compute flow solutions. CFX incorporates various turbulence models, multiphase flow models, heat transfer models, and other advanced features to capture and analyze complex fluid flow phenomena, like the boundary layer behavior, accurately. Considering the strengths and advantages previously mentioned, a detailed analysis is conducted using CFX to compare the results of the wingtip devices with those obtained from the VLM software. This allows a more comprehensive evaluation of the wingtip configurations and their respective aerodynamic performance.

VLM and CFD methods are used to perform and analyze the wingtip device designs, as they have been demonstrated to be convenient and accurate approaches for such studies. Initially, the base form of the wing is characterized with both VLM and CFD to have the baseline performance of the original wing. As a second stage, the VLM is employed to identify trends and approximate the most efficient winglet shape, taking advantage of the short time required to analyze each configuration and, therefore, the lower computational power required. Finally, the most promising designs found with VLM are evaluated and optimized using CFD software, providing more accurate results while properly capturing the boundary layer and viscous effects on the wing surface.

Improving the aerodynamic performance of a wing with minor changes, such as adding wing tip devices or wing extensions, has its limits. Significant changes may be necessary to achieve the best possible performance, affecting the construction process, materials, time, and cost. It is crucial to understand how much improvement can be attained with minor changes versus major ones, as this knowledge can help determine whether significant changes are feasible. Although this study focuses on enhancing performance by only implementing winglets or adding wing extensions, the results may suggest that the overall wing design needs to be reevaluated to meet the required performance characteristics.

There are more parameters to explore if the overall wing design needs to be optimized, such as searching for a more efficient and suitable airfoil. The wing planform could be optimized by varying the aspect ratio; taper ratio; sweep angle; dihedral, physical, or aerodynamic twist; and wing tip devices again.

THIS PAGE INTENTIONALLY LEFT BLANK

V. ORIGINAL BASELINE ANALYSIS

The first step in the search to improve the wing's aerodynamic efficiency is to characterize the baseline configuration. This is a design developed by the Mexican Navy and is an existing under-test configuration. The geometry of the UAV wing created in SolidWorks is presented in Figure 12, and its parameters are shown in Table 1.

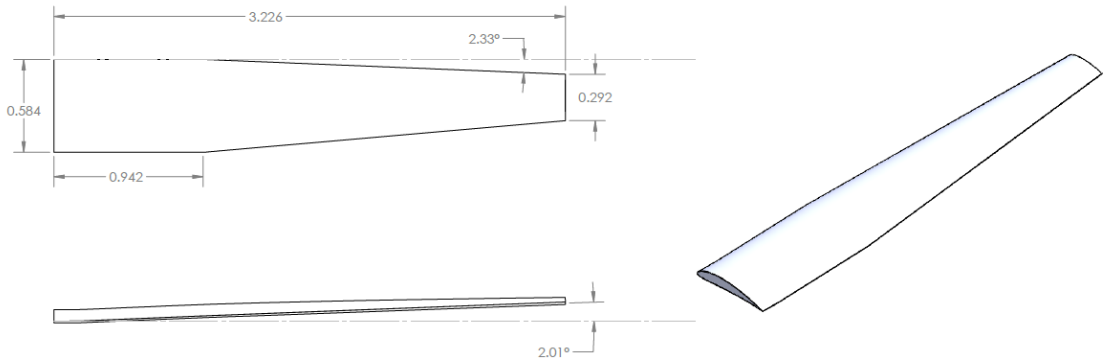

Figure 12. Half of the UAV wing created in Solidworks. Dimensions are in meters.

Table 1. Parameters of the UAV wing

Parameter	**Value**			
Wingspan	6.452 m			
Wing area	3.101 m²			
Projected area	3.100 m²			
MAC	0.5003 m			
Aspect ratio	13.4			
Taper ratio	0.5			
Section	Root	1	2	Tip
Chord	0.584 m	0.584 m	0.584 m	0.292 m
Dihedral angle	0°	2°	2°	2°
Twist	0°	0°	0°	-2.0°
Semi-span (b/2)	0 m	0.152 m	0.940 m	3.226 m
Sweep (c/4)	0°	0°	0.36°	0.36°
Airfoil	NACA6412-MH114			

The sections can be identified in Figure 15.

The airfoil used in the original design is an average of the NACA-6412 and the MH114, two profiles with similar shapes. The NACA-6412 has less camber, which results in a less complicated shape to manufacture, and the MH-114 provides better lifting characteristics. The complete study of this blended airfoil is beyond the scope of this work. The modification is performed in the Xflr5 software, and the resultant shape is shown in Figure 13. The resultant airfoil has a maximum thickness of 12.53% at 29.48% of the chord and a maximum camber of 6.26% at 43.98% of the chord.

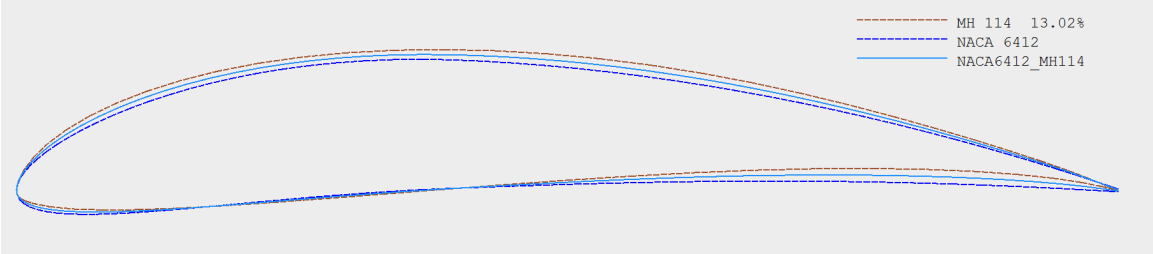

Figure 13. Interpolated airfoil from NACA-6412 and MH 114

The airfoil was analyzed using the Flow5 software, and the resultant polars are presented in Figure 14. The Reynolds numbers range from 500,000 to 1,300,000 to cover all the sections of the wing, from root to tip chord, which correspond to the average flight envelope of the UAV.

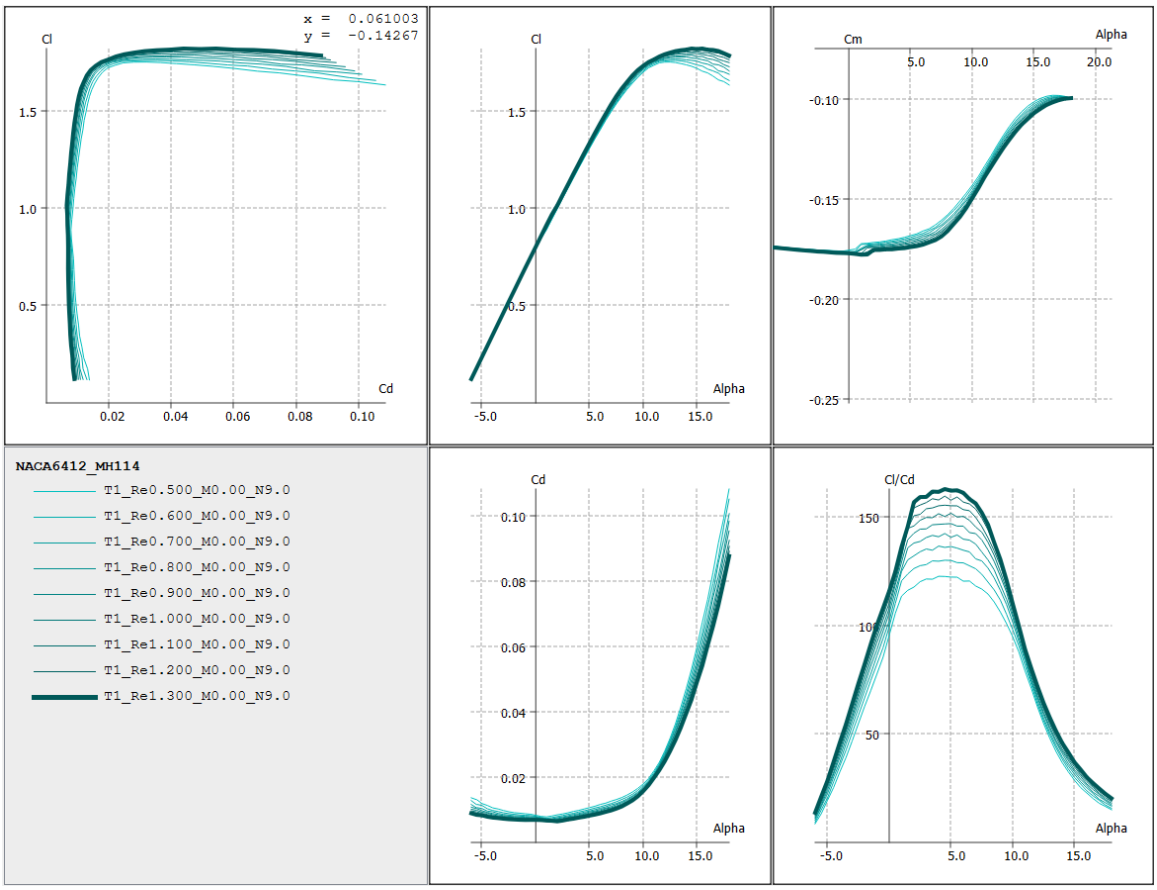

Figure 14. Polars of the NACA-6412–MH114 airfoil generated in Flow5

A. FLOW5 ANALYSIS

The wing's geometry, depicted in Figure 12, was rendered using the Flow5 software, following the procedure delineated in Appendix A. This geometric representation was constructed by employing three distinct sections for each semi-span. Given the wing's symmetry, capturing only half of the wing sufficed. The resulting geometry is illustrated in Figure 15.

Subsequent analysis leveraged the array of methods available within the Flow5 software, as comprehensively detailed earlier. The ensuing dataset is showcased in Figure 16, revealing a remarkable correlation among all the methods employed. Notably, the two VLMs, namely the horseshoe vortex (VLM1) and the ring vortex (VLM2), produced nearly identical results with negligible variation.

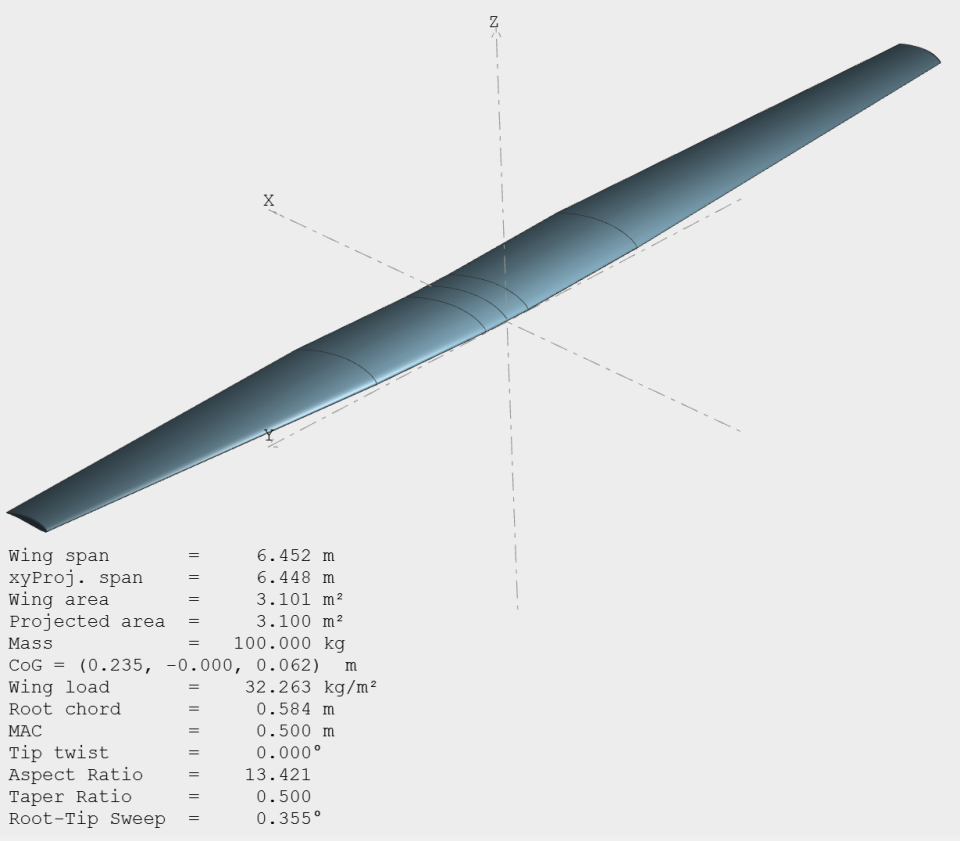

Figure 15. Geometry of the wing captured in Flow5 software

In contrast, the LLT method exhibited a significant underestimation of the overall drag. Consequently, the most promising methodologies emerged from the panel methods, which presented three distinct variants: uniform-density quad panels, uniform-density triangular panels, and linear-density triangular panels. From Figures 20, 21, and 22, I can conclude that the tri-uniform panel method is the one that most accurately computes the aerodynamics parameter when compared with CFX results.

The superiority of the triangular methods lies in their adeptness at representing 3D surfaces and significantly enhancing predictive accuracy, particularly in regions with high local pressure gradients. This finding underscores the potential and efficacy of employing such triangular panel methods in aerodynamic analyses and design considerations. These results are juxtaposed with the data obtained from the CFX analysis to determine the most suitable method for investigating potential wing modifications.

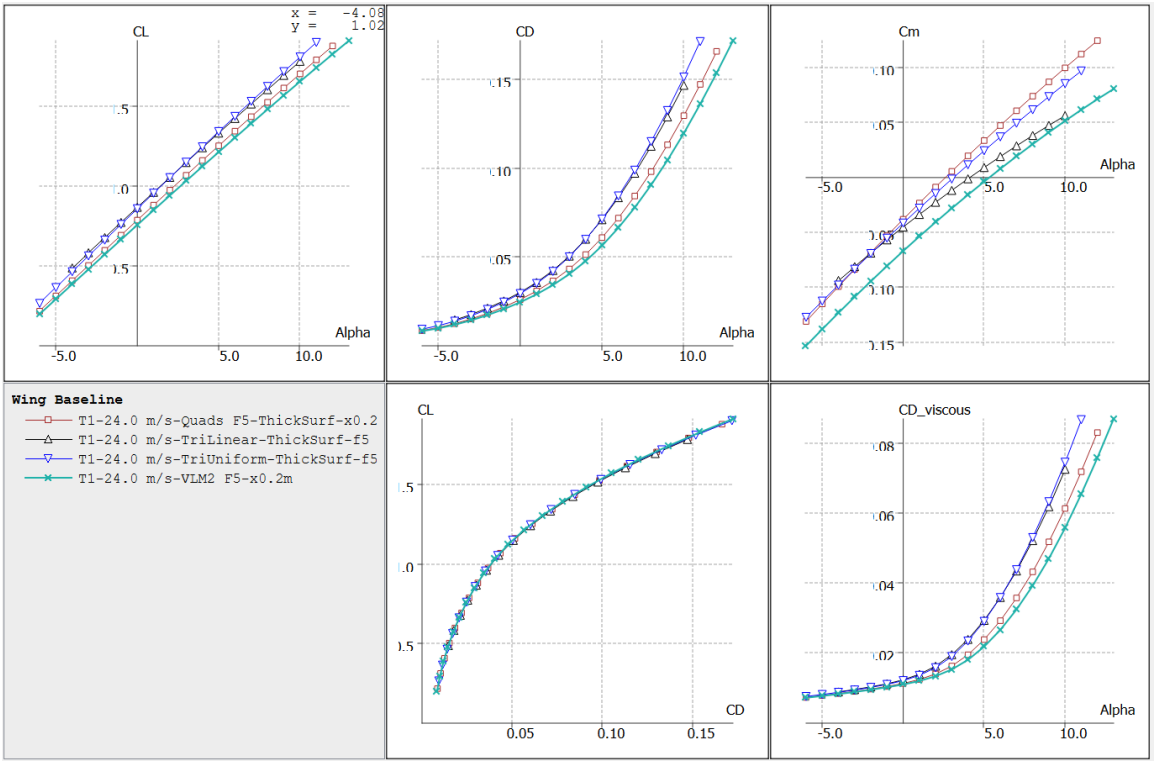

Figure 16. Polars of the UAV wing computed using the different methods available in Flow5, corresponding to 24 m/s velocity

B. CFD ANALYSIS

CFD software excels at analyzing the aerodynamic characteristics of a specific body within a particular fluid medium. In this study, CFX was employed to analyze the UAV wing illustrated in Figure 12, utilizing the parameters outlined in Table 1.

1. Wing Geometry and Fluid Domain

To streamline computation and enhance efficiency, the analysis focused on half of the wing within the fluid domain, considering both the wing and the fluid domain, as illustrated in Figure 17. The fluid domain extends one wingspan length to the front, top, and bottom sides, and it extends two wingspan lengths backward. To better control the mesh parameters and speed up the mesh generation, the fluid domain was strategically partitioned into four distinct subdomains, as depicted in Figure 17.

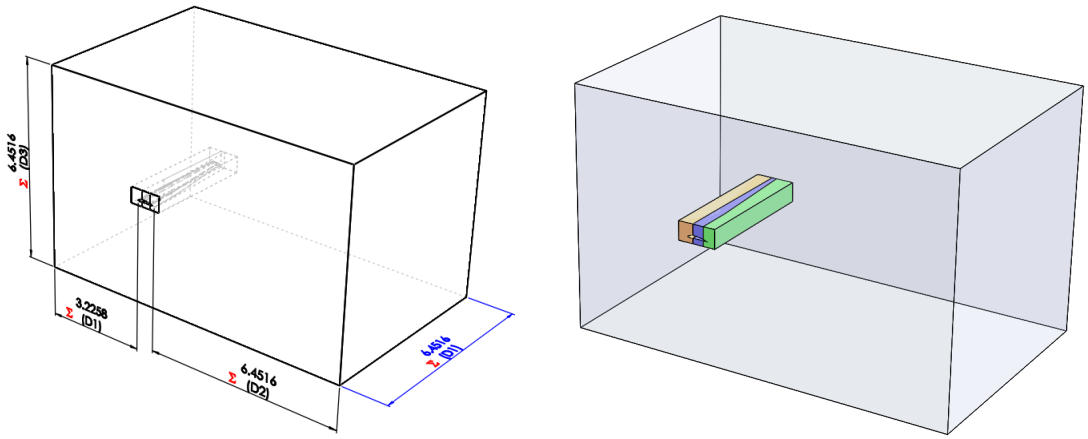

Figure 17. Fluid domain for the UAV wing (left) and blocks subdivision of the overall domain (right). Dimensions are in meters.

2. Mesh

Mesh generation is a critical initial step in CFD simulations. It involves dividing the domain of interest into smaller, discrete elements to solve the governing equations that numerically describe fluid flow and its behavior. The mesh's quality and appropriateness significantly impact the simulation's accuracy and efficiency.

When defining the mesh over the wing surface, it is important to be aware that changes in curvature result in changes in aerodynamic properties. For this reason, the advanced feature of capture curvature was applied to the wing surface. Additionally, I am interested in capturing the boundary layer effects on the wing surface. Therefore, an inflation method applied to all the wing surface is mandatory to capture this behavior appropriately. Since the Shear Stress Transport (SST) model was used as the turbulence model, the values of Y-plus need to be close to one. All of the adjustments and treatment to the mesh were done to conserve that value. The main settings applied to the mesh generation are presented in Table 2, and a detailed view of the final mesh over the wing profile is presented in Figure 18.

Table 2. Basic mesh settings applied to the baseline configuration

Parameter	Value
Sizing	
Element size	0.3 m
Growth rate	1.2
Curvature min size	4e-3 m
Curvature normal angle	0.5 degrees
Inflation	
Inflation option	First layer thickness
First layer height	4e-6
Maximum layers	36
Growth rate	1.2
Statistics	
Nodes	13834606
Elements	30946681

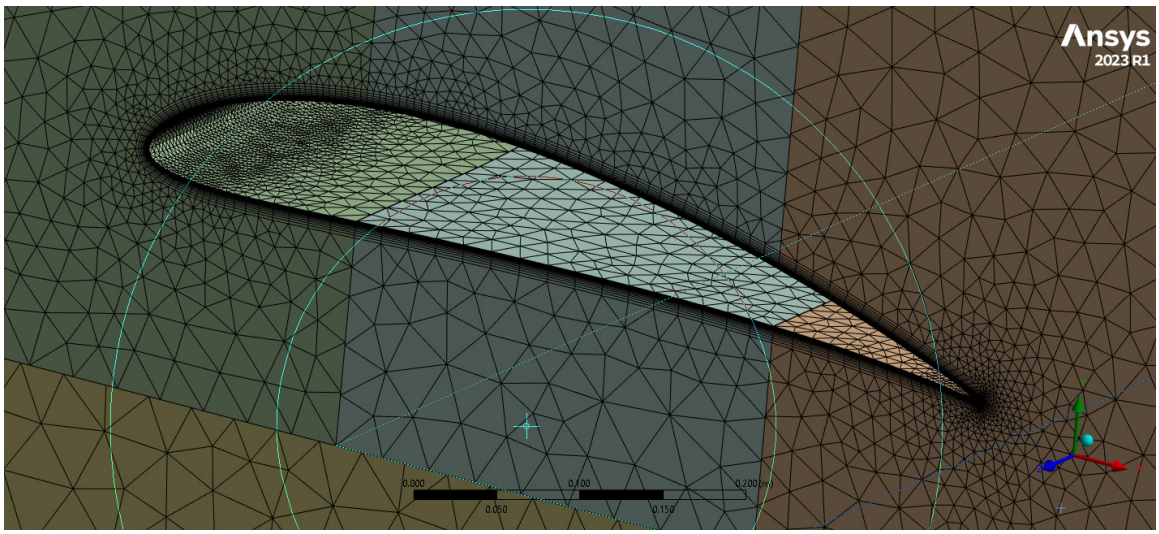

Figure 18. Mesh generated over the wing surface

3. Solution Setup

On the CFX-Pre interface, the solution setup is configured. The configuration of parameters like the material, the fluid models governing the simulation and the boundary conditions need to be specified.

a. Default Domain

In the default domain, it is necessary to specify the fluid domain corresponding to the main solid imported as the geometry since these flight conditions correspond to a low-speed simulation where the assumption of incompressible flow is appropriate. The SST option is selected for the turbulence model. It is challenging to accurately predict flow separation from a smooth surface in turbulence models, particularly under adverse pressure gradient conditions. This phenomenon is important to capture in this analysis. The $k-\omega$ based SST model was created to accurately predict the onset and extent of flow separation in adverse pressure gradients through incorporating transport effects into the eddy-viscosity formulation. [29]. Fully turbulent and transitional flow were tested, and similar results were obtained. Therefore, the SST model was used to analyze the wing configurations.

b. Boundary Conditions

Some named selections were created to identify and designate the boundary conditions in the domain. Similarly, expressions were established to characterize the main parameters describing the geometry and boundary conditions.

The wing was analyzed at 24 m/s, which corresponds to the cruise velocity identified during flight tests. Angles of attack (AoAs) between -3 and 12 degrees were considered. For non-zero AoAs, the inlet velocity vector and inlet/outlet faces were adjusted as needed to avoid modifying the geometry and mesh for each scenario. The boundary conditions specified for the baseline wing configuration are shown in Figure 19.

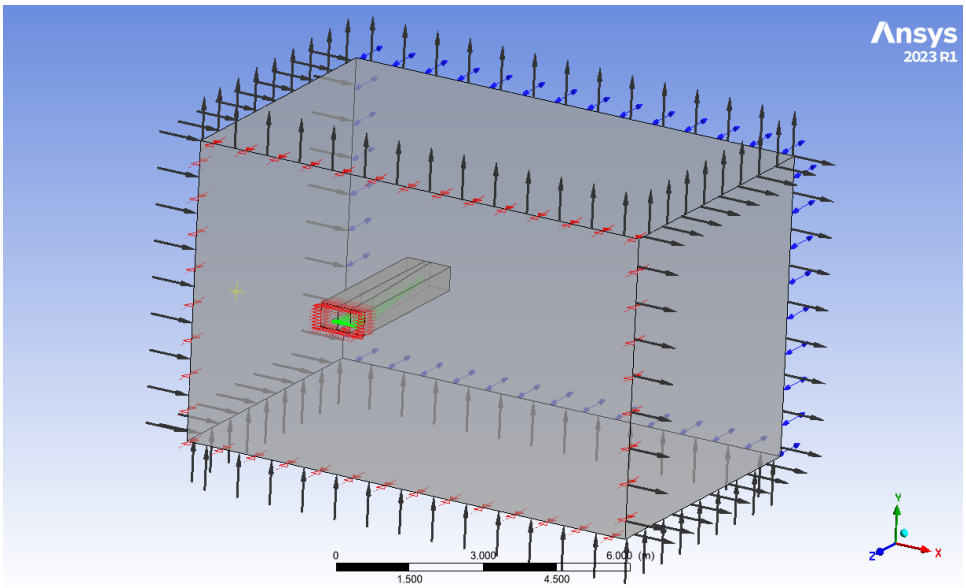

Figure 19. Boundary conditions applied to the fluid domain

Besides the behavior of the fluid passing the wing at different spots, I am interested in computing the forces and moments developed by the wing to analyze them and compare them with those obtained from the Flow 5 software. Some expressions were created to calculate the most characteristic coefficients, lift coefficient (***Cl***), drag coefficient (***Cd***), pitching moment coefficient (***Cm***), and bending moment coefficient ***(Cbm)***:

- ***Cl*** is computed with expression: ***Lift*** */(Qinf* S)*
- ***Cd*** is computed with expression: ***Drag*** */(Qinf* S)*
- ***Cm*** is computed with expression: *torque_z@Wing/(Qinf* S *Cref*)
- ***Cbm*** is computed with expression: *torque_x@Wing/(Qinf* S *Lref*)
- **Lift** is computed with expression: force_y*cos(AoA)-force_x*sin(AoA)
- **Drag** is computed with expression: force_y*sin(AoA)+force_x*cos(AoA)

where *Qinf* corresponds to dynamic pressure, *S* is the projected area of the wing, since only half of the wing is analyzed $S = 1.55\ m^2$, *Cref* corresponds to the mean

aerodynamic chord (MAC) value equal to 0.5003 m, and *Lref* corresponds to the semispan value equal to 3.226 m.

c. Solution Procedure

While defining the run in the Solver Manager interface, some options need to be configured to ensure a proper solution. In Run settings, the ***Double Precision*** was selected to determine the precision of the partitioner, solver, and interpolator executables. The initial values were set to ***Initial Conditions***.

Convergence criteria vary based on the simulation's purpose and model details. Residual size, flow balances, and relative quantity sensitivity testing are key factors to consider for quantitative accuracy. In computational fluid dynamics, the residual is a crucial metric that measures the local imbalance of each conservative control volume equation. It serves as a primary indicator of whether the equations have been solved accurately or not. To judge convergence, CFX employs normalized residuals, which provide a relatively consistent basis for assessing convergence by standardizing the residuals [30].

4. Results

To capture the behavior at different flight conditions, the simulation was run at different AoAs, ranging from -3 to 12 degrees, in steps of 3 degrees. The resultant **Cl**, **Cd**, **Cm,** and the bending moment plots are presented in Figures 20, 21, 22, and 23, respectively. Additionally, the same plots provide the values obtained from Flow5 software to contrast the fidelity between the two methods.

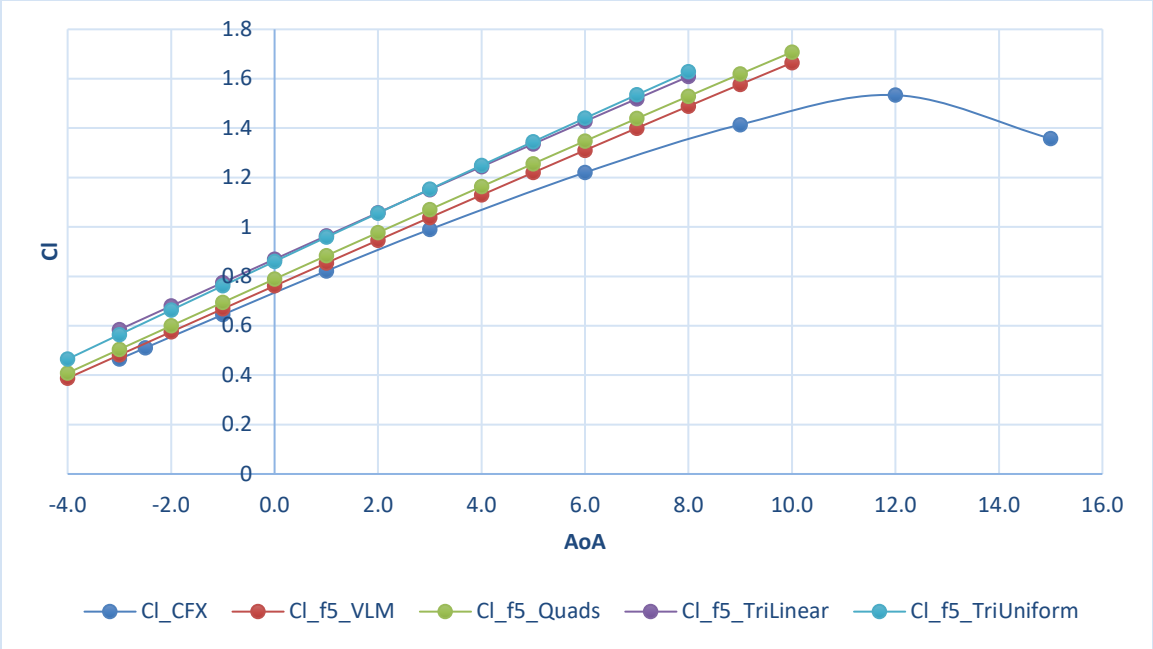

Figure 20. Comparison of the wing lift coefficient between data from CFX and data from Flow5 at 24 m/s velocity

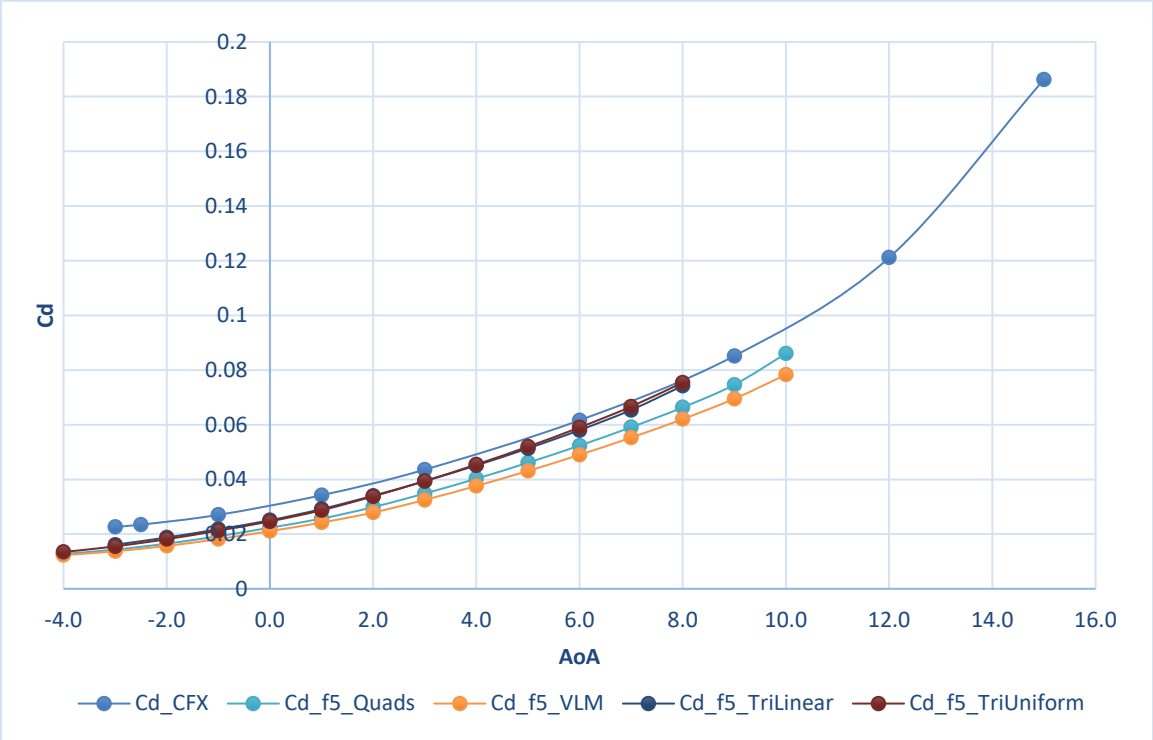

Figure 21. Comparison of the wing drag coefficient between data from CFX and data from Flow5 at 24 m/s velocity

The lift coefficient is overestimated by the methods available on Flow5 software, as depicted in Figure 20. The VLM is the method that has the closest relationship with the CFX data. Prieto et. al [17] found on previous studies that the methods used on Xflr5, now implemented in Flow 5, overestimate the lift by 1%–5%, and the opposite happens with the estimation of the induced drag, resulting in 20% underestimation. These effects agree with the data presented in Figure 20 and Figure 21.

The estimation of the drag coefficient is more precise with the uniform triangular panel method, as depicted in Figure 21. Since the bending moment is directly related to the lift coefficient, a similar trend can be observed in Figure 23, where again the VLM provides the most accurate calculation.

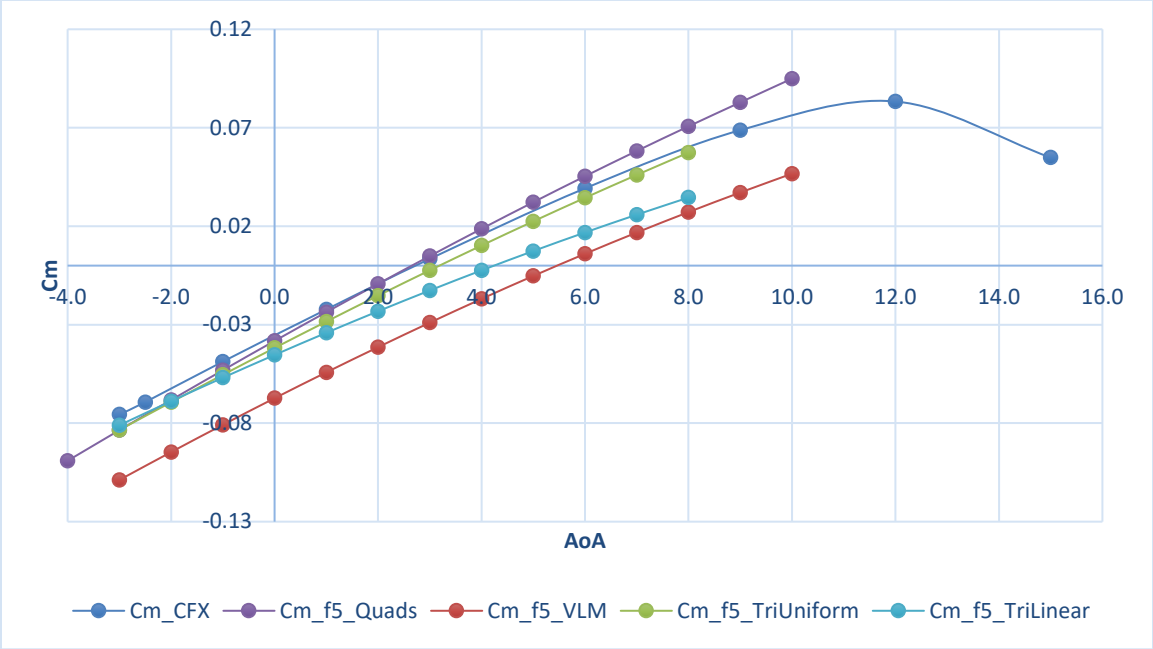

Figure 22. Comparison of the wing moment coefficient between data from CFX and data from Flow5 at 24 m/s velocity

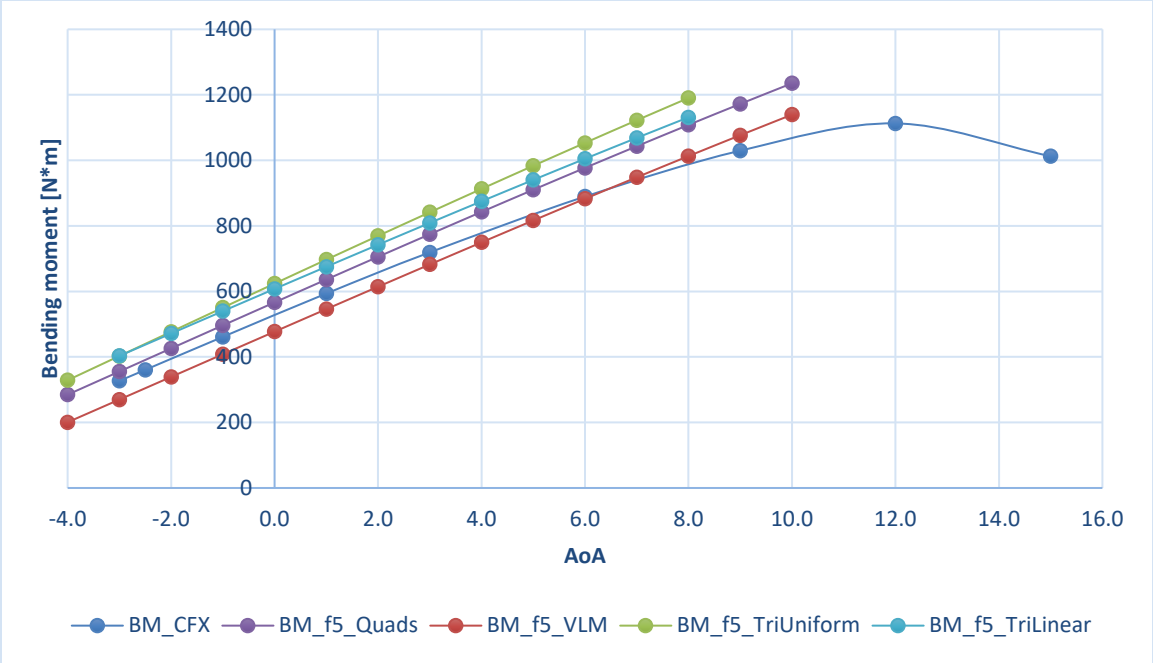

Figure 23. Comparison of the wing bending moment between data from CFX and data from Flow5 at 24 m/s velocity

In general, the precision of the low-fidelity numerical methods is as expected according to previous studies in this field. This low precision is enough to explore different wing configurations while looking for improvements in the aerodynamic efficiency of the wing. The final configurations found in Flow5 are analyzed with CFX to more precisecly capture the viscous effects and boundary layer behavior.

The focus of this study is the reduction of the induced drag. From previous sections, it is known that this type of drag is represented mainly with the tip vortex formation. Therefore, an interesting spot to focus on is the wing tip to investigate the vortex formation, strength, and size. Figure 24 shows the vortex formation on the wingtip.

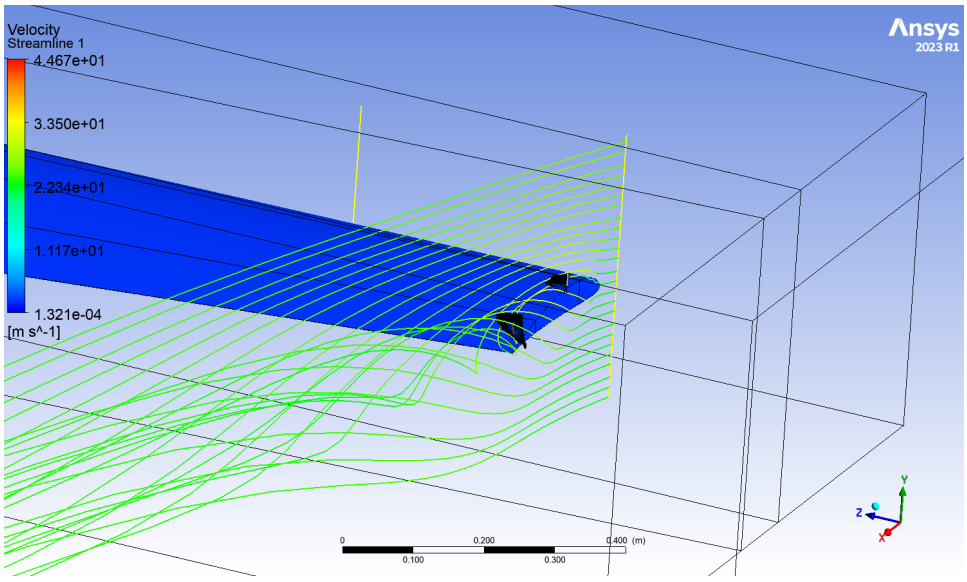

Figure 24. Vortex formation on the wingtip at 9 degrees of AoA as calculated by CFX

The precision of these results is dependent on the parameter Y-plus, which for this specific case needs to be less than one because I am applying the SST turbulence model. To get a value close to this parameter, different iterations were necessary to develop, varying the initial height of the inflation layer and the minimum element size in the curvature control. The Y-plus value along the wing surface is shown in Figure 25. There are minor spots where the Y-plus value is greater than one, most of them on the leading edge of the wing.

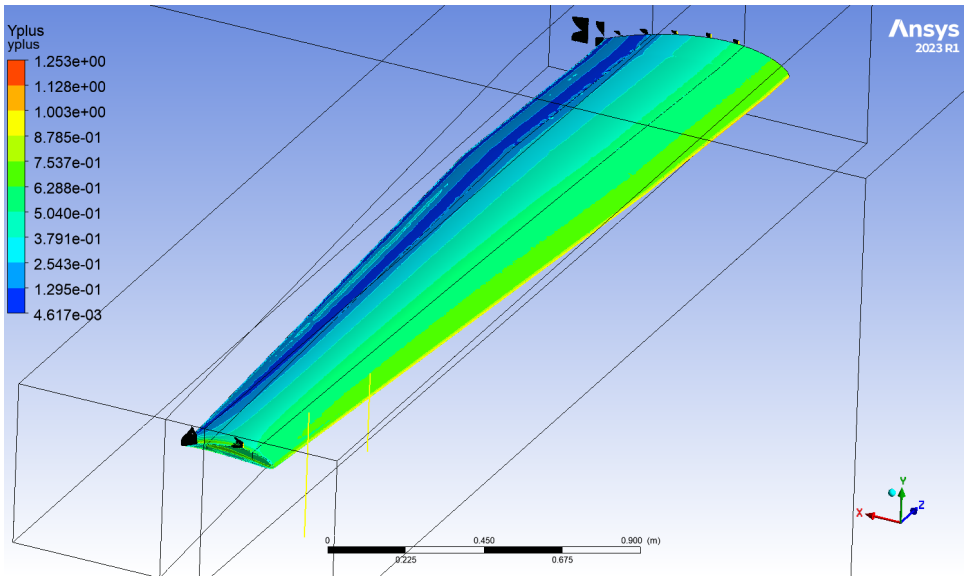

Figure 25. Y-plus parameter along the wing surface

THIS PAGE INTENTIONALLY LEFT BLANK

VI. WING MODIFICATIONS ANALYZED IN FLOW5

Three different modifications are explored to look for improved wing performance. The first is a wing extension of 10% of the wingspan. In this configuration, the dihedral angle and sweep angle are maintained. The second option is the implementation of a raked wingtip. This is like the wing extension, but parameters like sweep angle, dihedral angle, and taper ratio are tested to find the configuration with better performance. The last option is the blended winglet, where the cant angle plays a vital role in the final configuration's effectiveness and the airfoils that need to be revised.

A. WING EXTENSION

The first option to explore, looking to improve the wing's aerodynamic efficiency, is the implementation of wing extensions. A restriction of a 10% increase for the wingspan is established to compare this configuration with the others. This extension was added to the wing, maintaining the same sweep angle and twist on the wingtip. The geometry was captured on Flow5 software to characterize its performance. The resultant geometry is depicted in Figure 25 in contrast with the initial configuration. The resultant geometric parameters are described in Table 3.

Table 3. Parameters of the UAV wing with 10% wing extension

Parameter	**Value**				
Wingspan	7.742 m				
Wing area	3.425 m²				
Projected area	3.423 m²				
MAC	0.477 m				
Aspect ratio	17.5				
Taper ratio	0.359				
Section	Root	1	2	3	Tip
Chord	0.584 m	0.584 m	0.584 m	0.292 m	0.210
Dihedral angle	0°	2°	2°	2°	2°
Twist	0°	0°	0°	-2°	-3°
Semi-span (b/2)	0 m	0.152 m	0.940 m	3.226 m	3.871 m
Sweep (c/4)	0°	0°	0.36°	0.36°	0.36°
Airfoil	NACA6412-MH114				

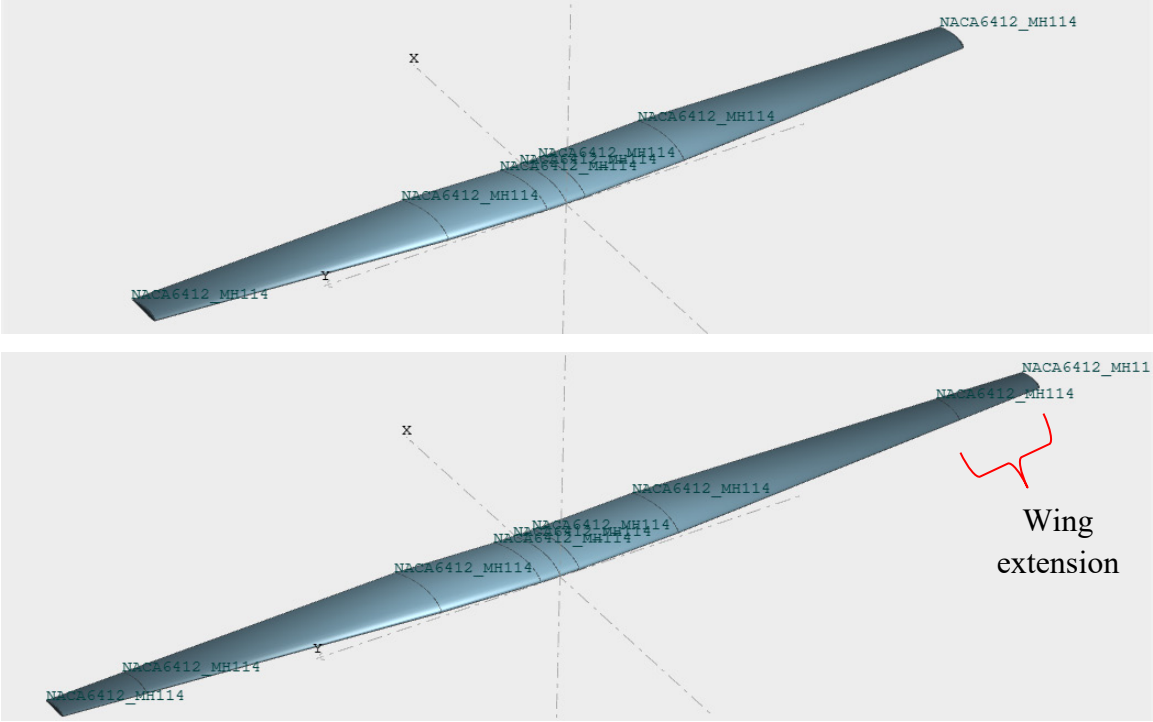

Figure 26. Comparison between the original baseline geometry of the UAV wing (top) with the configuration of 10% wing extension (bottom)

The resultant aerodynamic coefficients are presented in Figure 27, where the improvement concerning the baseline configuration is visible. The Cl/Cd ratio improvement comes mainly from the reduction of induced drag and, therefore, total drag. The difference in the lift coefficient is slight but also contributes to the increase in aerodynamic efficiency. Leishman [31] states that higher aspect ratios result in higher lift-to-drag ratios, as seen in Figure 28. Therefore, the augmented aspect ratio, which changed from 13.5 to 17.5, is the main contributor to this improvement in wing efficiency.

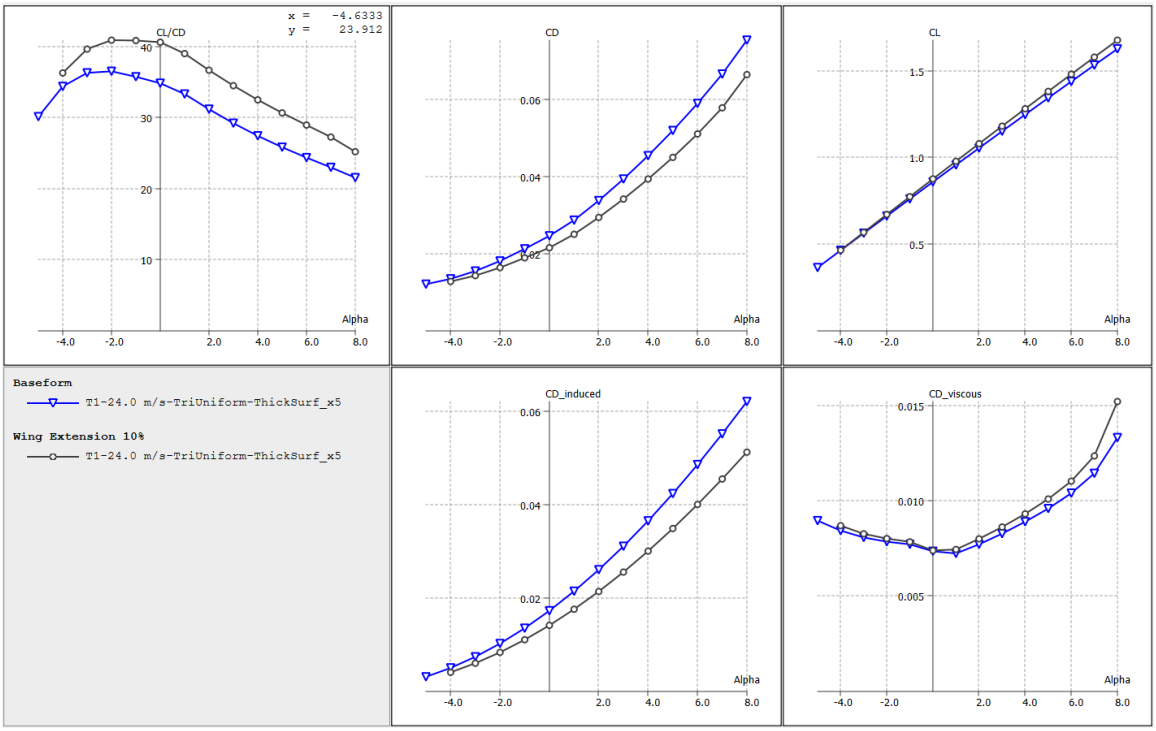

Figure 27. Comparison of the aerodynamic coefficients between the baseline configuration and the 10% wing extension

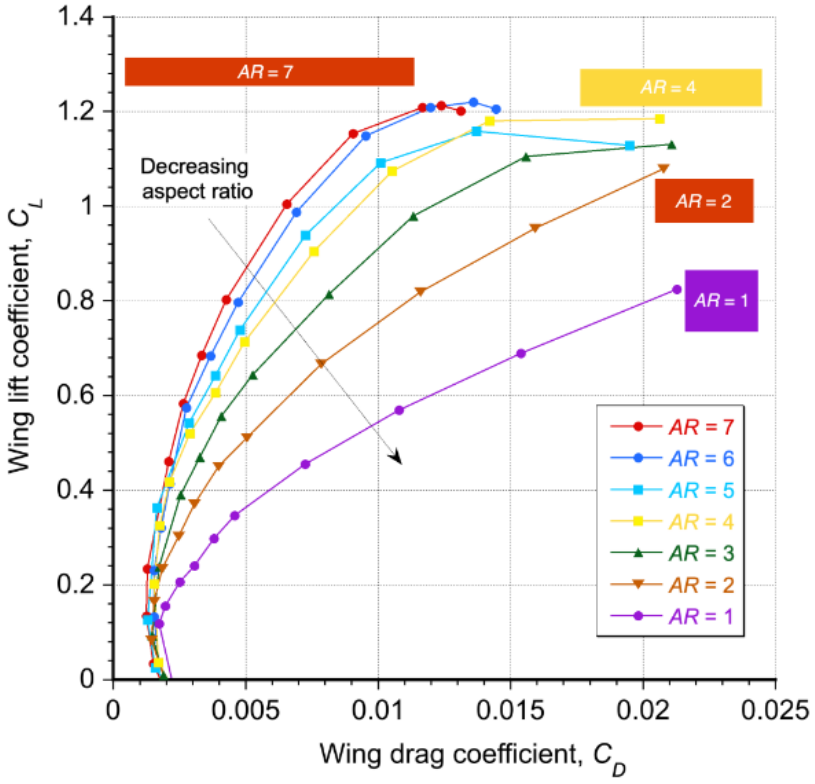

Figure 28. Effect of the wing aspect ratio on the lift-to-drag ratio. Source: [31].

B. RAKED WINGTIP

Raked wingtips are a type of wingtip device like a wing extension, with a raked angle, like sweep, but measured on the wing's leading edge. Additionally, they have a lower taper ratio than a standard wing and dihedral angle only applied to the raked wingtip, as shown in Figure 29. This type of device is not a novel configuration; Norton [32] first studied it in 1921. This study found that the raked angle directly affected the lift coefficient, but only to a maximum value of 30 degrees. The study also found that the significant effect of the raked wingtips was at low AoA. This last point was also concluded by Mahmood and Das [33], who found that the L/D ratio was best from 0 to 4 degrees of AoA. This fact is interesting because I am looking for devices to operate more efficiently in cruise flight conditions. It is worth mentioning that there is a similar effect whether the rake angle is positive or negative.

Regarding the dihedral angle, Gudmunson [34] found that from 4 to 8 degrees is a reasonable range to search for optimal performance of the raked wingtip.

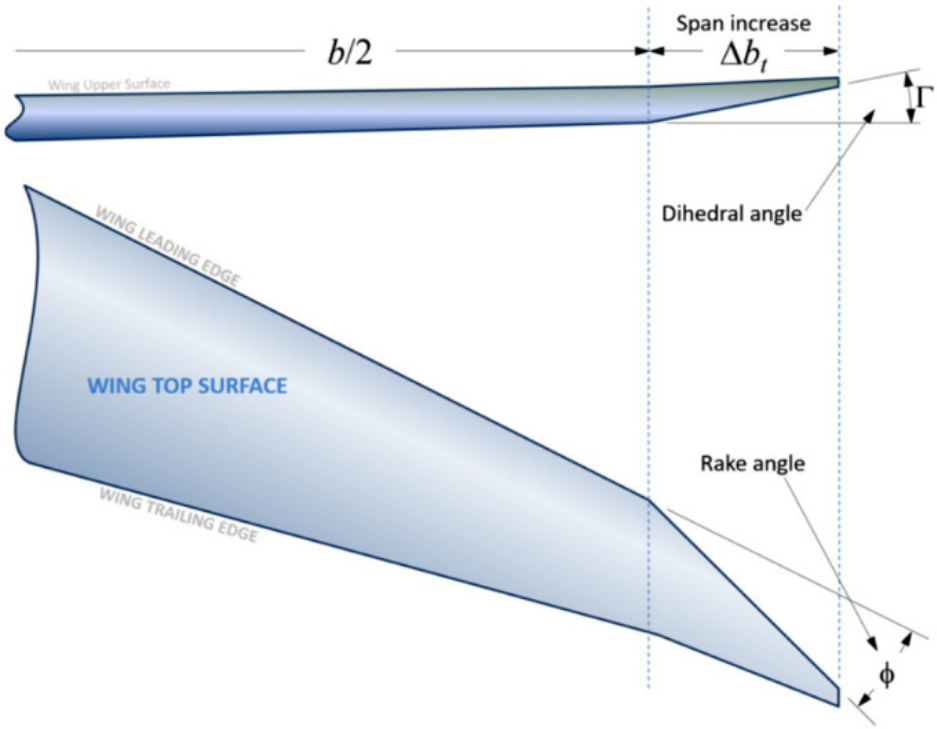

Figure 29. Parameters defining the raked wingtip. Source: [34].

The exploration of the previous parameters was performed on Flow5 software. Table 4 presents the parameters and ranges explored.

Table 4. Raked wingtip parameters and their boundaries

Parameter	**Min value**	**Max value**
Semispan increase	10% (0.3226 m)	20% (0.6452 m)
Rake angle	0°	30°
Dihedral angle	0°	20°
Taper ratio	0.3 (0.0876 m)	0.7 (0.2045 m)
Tip twist	-5°	5°

1. Optimization of Parameters

Flow5 has an optimization module based on the algorithm of particle swarm optimization (PSO) [35]. The complete explanation of this and similar methods are beyond the scope of this work. The functionality of this type of algorithm is the exploration of different parameters while trying to achieve a specific goal parameter. Multiple-objective particle swarm optimization (MOPSO) algorithms also exist. These are an improvement to the PSO algorithm because multiple objectives can be optimized at once. For example, I can attempt to reach the best lift-to-drag ratio while reducing the pitching moment. In the end, the goals can be achieved for more than one unique configuration forming the Pareto frontier, like the one presented in Figure 30.

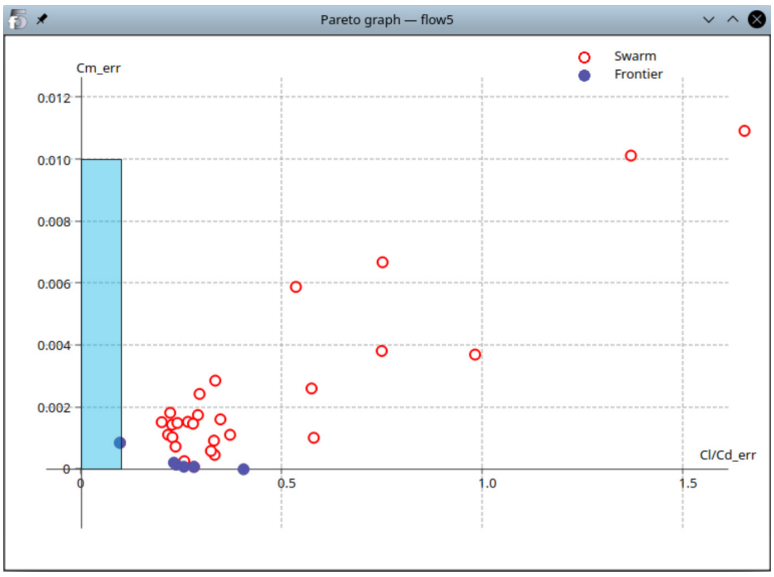

Figure 30. Example of formation of the Pareto frontier using Flow5 optimization module. Source: [36].

The parameters specified in Table 4 were explored using the optimization tool incorporated in Flow5 following the process stated in Appendix B. The software performs the MOPSO algorithm to look for the higher L/D ratio while minimizing the drag. After completing 100 iterations, the software delivers the resultant parameters, as shown in Figure 31, where the final parameters, the objective optimized values, and the

Pareto frontier are presented. As depicted in Figure 31, more than one configuration could give similar results in the objective values, and an exploration of each parameter is necessary to define the most convenient geometry. The final parameters are presented in Table 5.

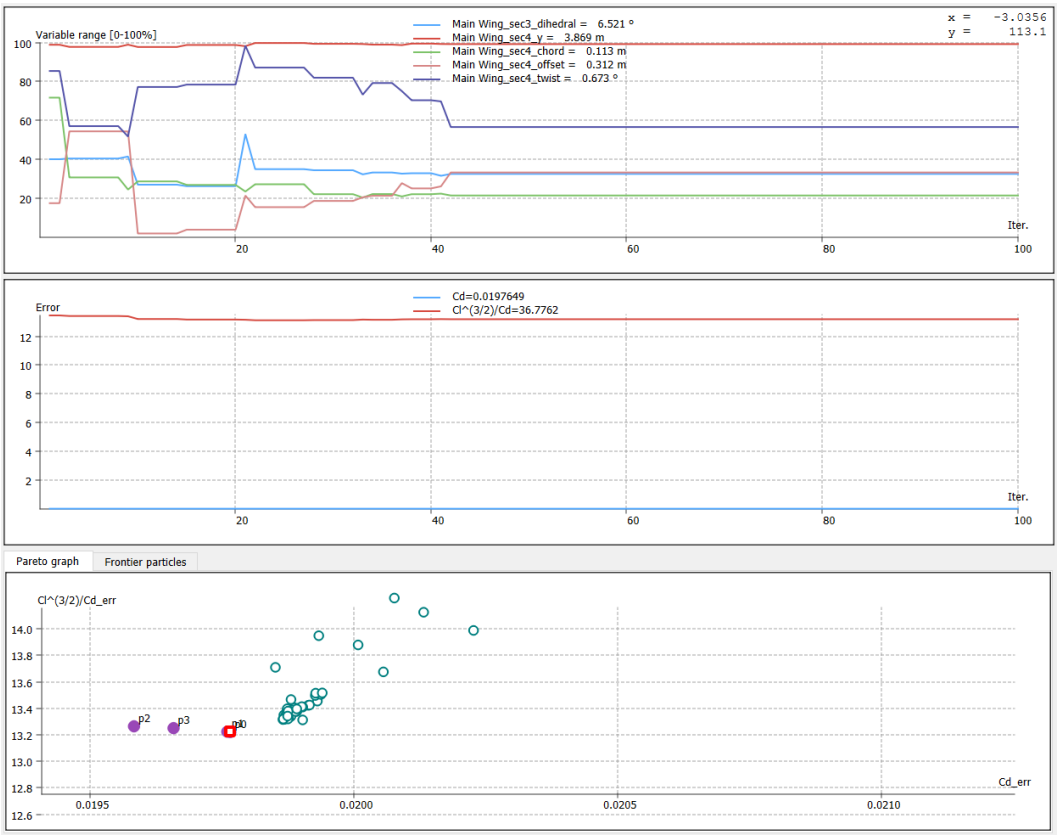

Figure 31. Flow5 results of the optimization process, where the final parameters (top), the goal values (middle), and the Pareto frontier (bottom) are shown

Table 5. Raked wingtip parameters boundaries and the resultant optimum values from Flow5 software

Parameter	Min value	Max value	Optimum value
Semispan increase	10% (0.3226 m)	20% (0.6452 m)	20% (0.6452 m)
Rake angle	0°	30°	15°
Dihedral angle	0°	20°	6.521°
Taper ratio	0.3 (0.0876 m)	0.7 (0.2045 m)	0.4 (0.113 m)
Tip twist	-5°	5°	0.673°

2. Winglet Airfoil

Implementing a new profile on the winglet tip was explored to improve the aerodynamic performance even more. Maughmer et al. [37] designed a promising profile, the PSU 94–097, explicitly for winglets operating in a wide range of low Reynolds numbers. The airfoil shape and its inviscid velocity plot are presented in Figure 32.

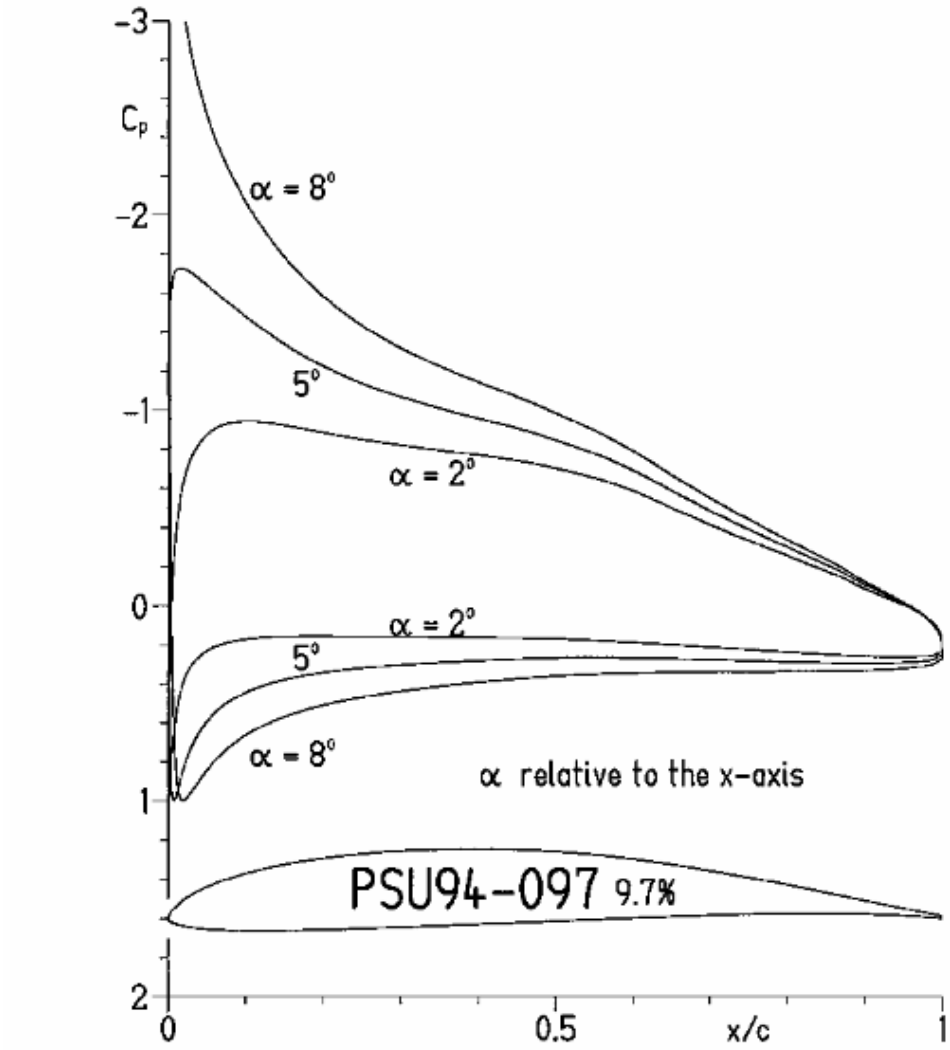

Figure 32. PSU 94–097 airfoil and inviscid velocity distributions at different AoAs. Source: [37].

This airfoil was implemented in the optimum configuration, resulting in a slightly higher L/D ratio.

The resultant shape of the wing with the addition of the raked winglet is presented in Figure 33. The plots of the aerodynamic coefficient are depicted in Figure 34, where a comparison with the original baseline configuration can be seen. As expected, reasonable improvement is noticeable in the plots. The higher L/D ratios come mainly from the reduction in the induced drag.

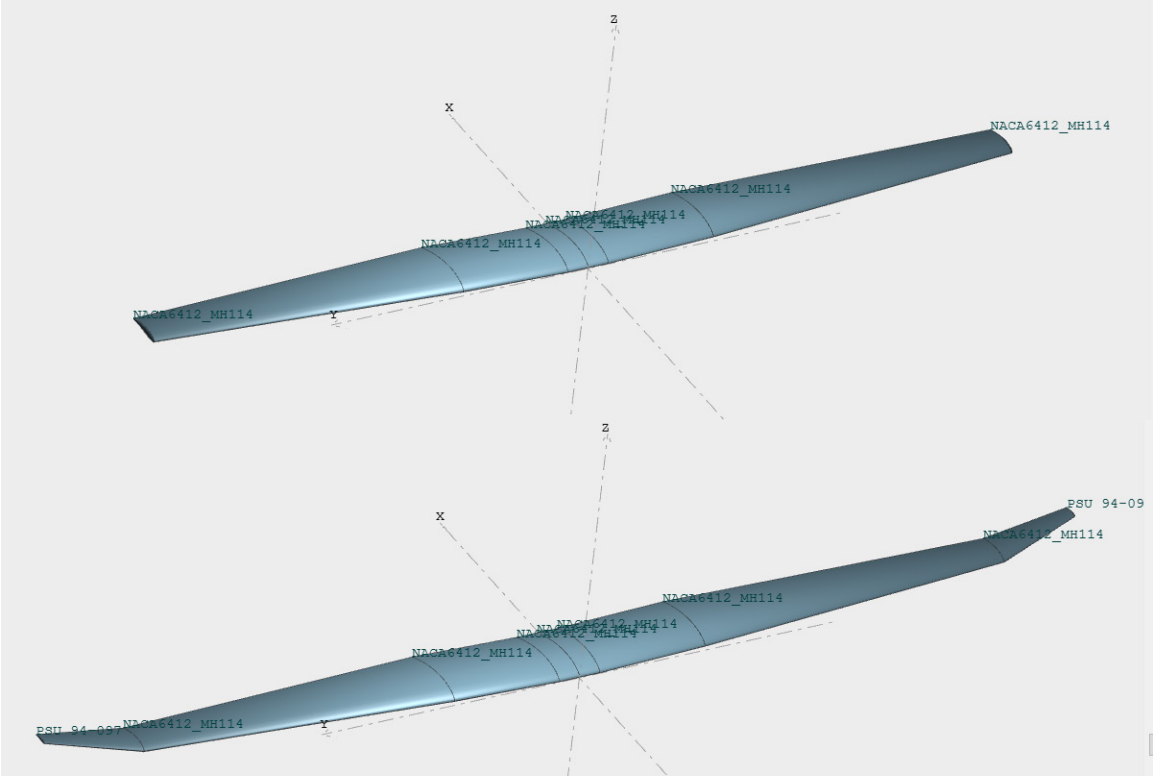

Figure 33. Comparison between the original baseline geometry of the UAV wing (top) and the configuration with the raked wingtip (bottom)

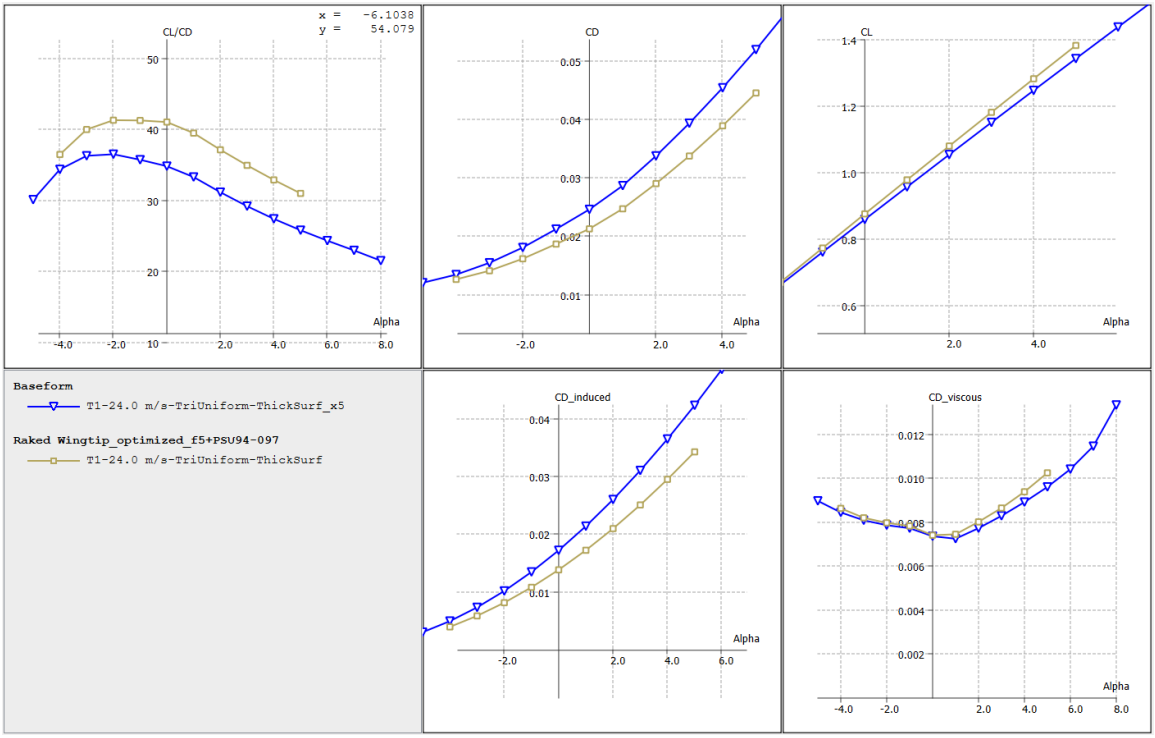

Figure 34. Aerodynamic coefficients of the original baseline geometry of the UAV wing compared with the raked winglet configuration

C. BLENDED WINGLET

Louis B. Gratzer was the designer of the blended winglets [34]. This winglet type is characterized by a blended transition from the wing to the winglet, where the blend radius is higher than a normal winglet. As depicted in Figure 35, the main parameters defining its geometry are the sweep angle, cant angle, twist angle, blend radius, length, and taper ratio. Different studies have been carried out to optimize this type of winglet. The optimized geometry depends on the aircraft's type and operation parameters, but some general conclusions have been established regarding its performance.

Madhanraj et al. [38] and Makgantai et al. [15] found that a cant angle of 60 degrees delivers the best L/D ratio. Similar results were found by Panagiotou et al. [39], who performed a study using CFD and found that the implementation of blended winglets can increase the endurance by 10% with minor changes in stalling and pitching stability, again with a cant angle between 50–60 degrees.

The length of the winglet is another critical parameter that highly affects its performance. Actually, the length and the cant angle are the most critical parameters to explore in this type of winglet, as they have a more significant effect on the overall performance [40]. Since there is a limit for a maximum increase of the wingspan of 10%, the maximum length of the winglet is limited by this fact. Halpert et al. [41] found that the radius of transition should be about 50% of the winglet length for best results. Following this recommendation, the radius was fixed with that parameter.

The remaining parameters to explore are the length, cant angle, twist angle, sweep angle, and aspect ratio of the winglet. These parameters and their boundaries are specified in Table 6. The exact change was made in the blended winglet because some improvement was achieved when changing the tip airfoil of the raked wingtip for the PSU94-097 airfoil.

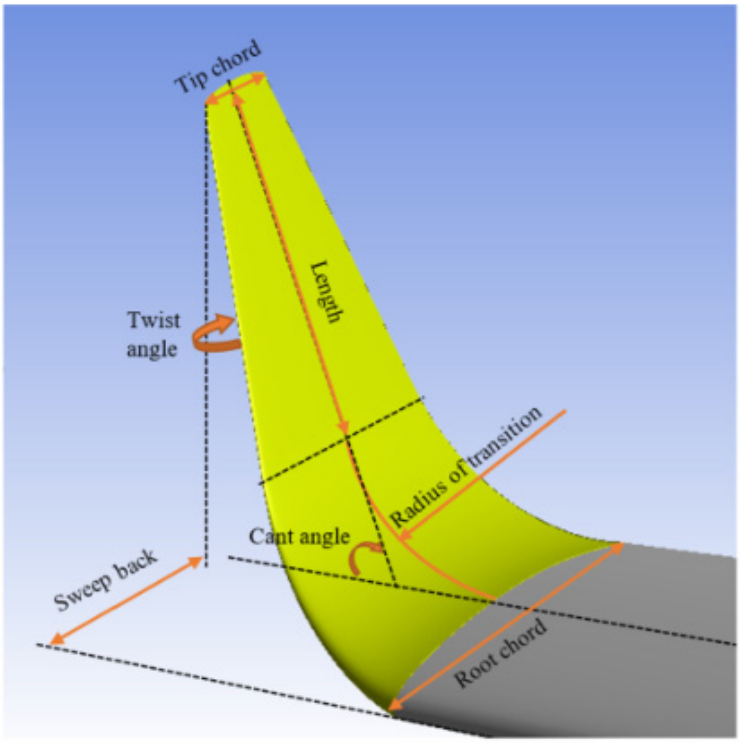

Figure 35. Parameters defining the geometry of the blended wingtip. Source: [42].

Table 6. Blended wingtip parameters and their boundaries

Parameter	Min value	Max value
Length	0.2 m	0.55 m
Cant angle	55°	65°
Sweep angle	15°	50°
Taper ratio	0.3 (0.0876 m)	0.7 (0.2045 m)
Twist angle	-5°	5°

The same procedure to optimize the parameters of the raked wingtip was performed on the optimization module of the Flow5 software. The resultant parameters and geometry are presented in Figure 36 and Table 7, respectively.

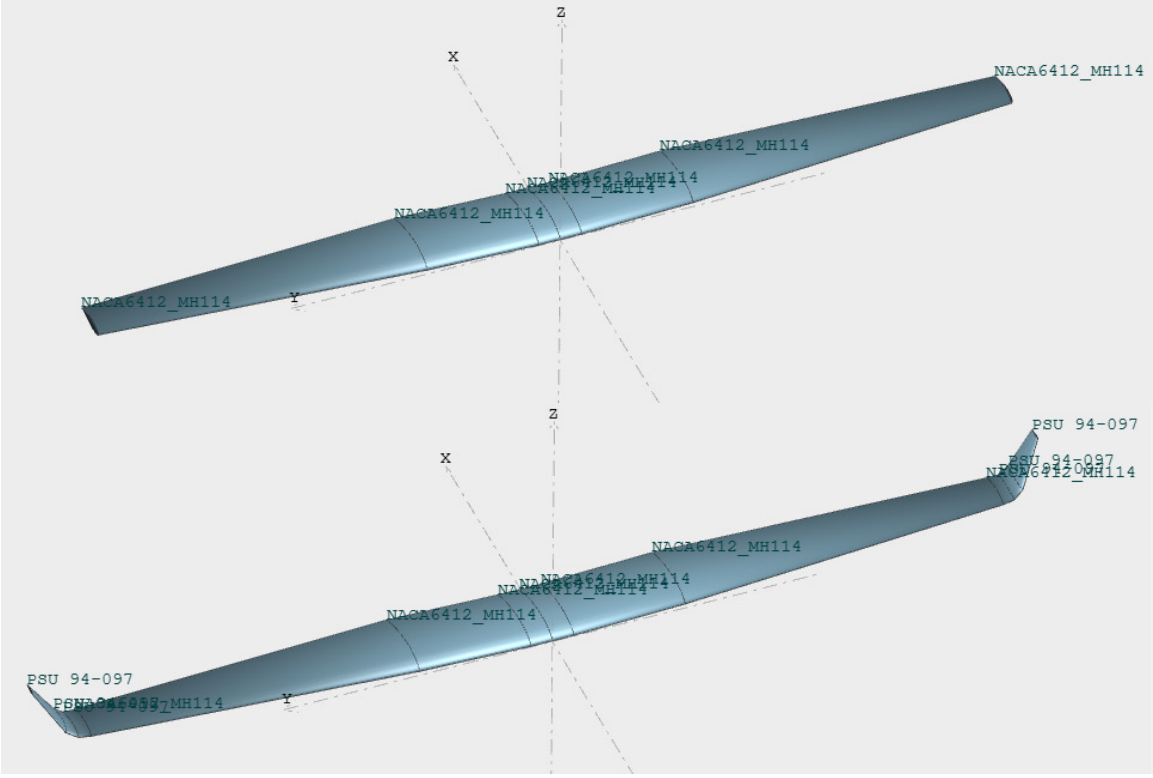

Figure 36. Comparison between the original baseline geometry of the UAV wing (top) and the configuration with the blended winglet (bottom)

Table 7. Blended wingtip parameters boundaries and the resultant optimum values from Flow5 software

Parameter	Min value	Max value	Optimized value
Length	0.2 m	0.55 m	0.3236
Cant angle	50°	65°	55°
Sweep angle	15°	50°	40°
Taper ratio	0.3	0.7	0.3
Twist angle	-5°	5°	-4

The resultant aerodynamic coefficients of blended winglet configuration are presented in Figure 37.

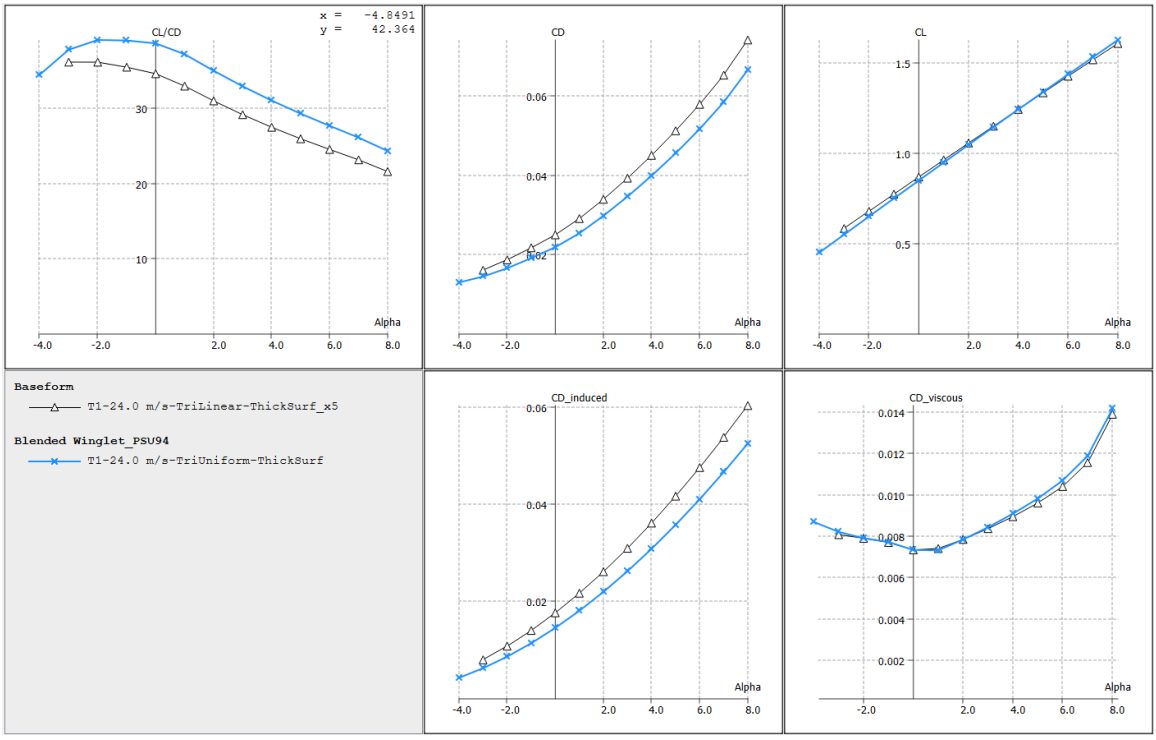

Figure 37. Aerodynamic coefficients of the original baseline geometry of the UAV wing compared to the blended winglet configuration

It is notable a considerable increase in the L/D ratio coming mainly from the reduction of the drag, specifically the induced drag, Since the lift coefficient and viscous drag do not change significantly. An interesting fact to note is that at low AoA, the

blended winglet configuration has a lower lift coefficient compared with the baseline configuration.

D. COMPARISON BETWEEN THE ANALYZED CONFIGURATIONS

Four different configurations of the wing were analyzed using Flow5 software. The first is the original baseline configuration, for which I am looking to improve its performance by adding wingtip devices. The second consist of adding a wing extension of 10% of the wingspan. The third option is an implementation of a raked wingtip, again limiting the wingspan increase to the same amount of the wing extension. The final configuration is the inclusion of a blended wingtip. The geometry of the four configurations is presented in Figure 38, focusing mainly on the tip of the wing where the modifications were done to best compare the changes.

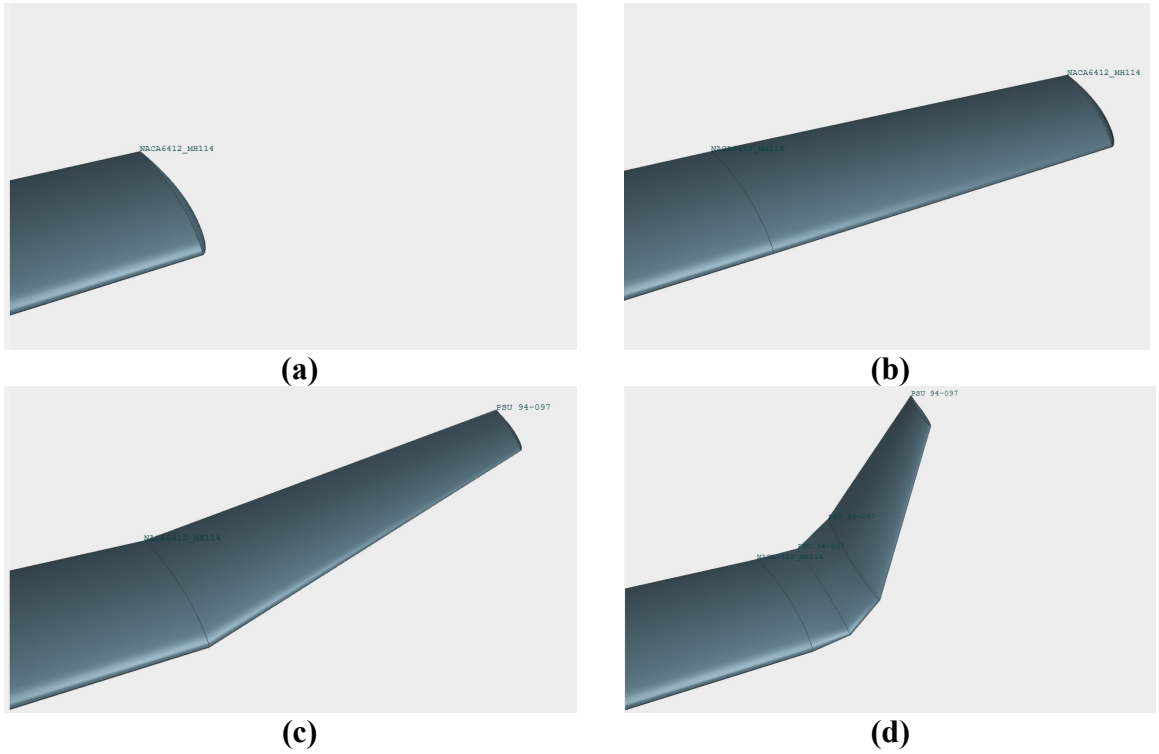

Figure 38. Comparison of the four wingtip configurations: baseline geometry (a), wing extension (b), raked wingtip (c), and blended winglet (d)

The aerodynamic coefficient for all four configurations is presented in Figure 39. The three modified wingtips explored result in an improvement of the aerodynamic efficiency of the wing. The raked wingtip achieved the best performance, which is very close to the wing extension. However, the bending moment is slightly higher for the wing extension than it is for the raked wingtip.

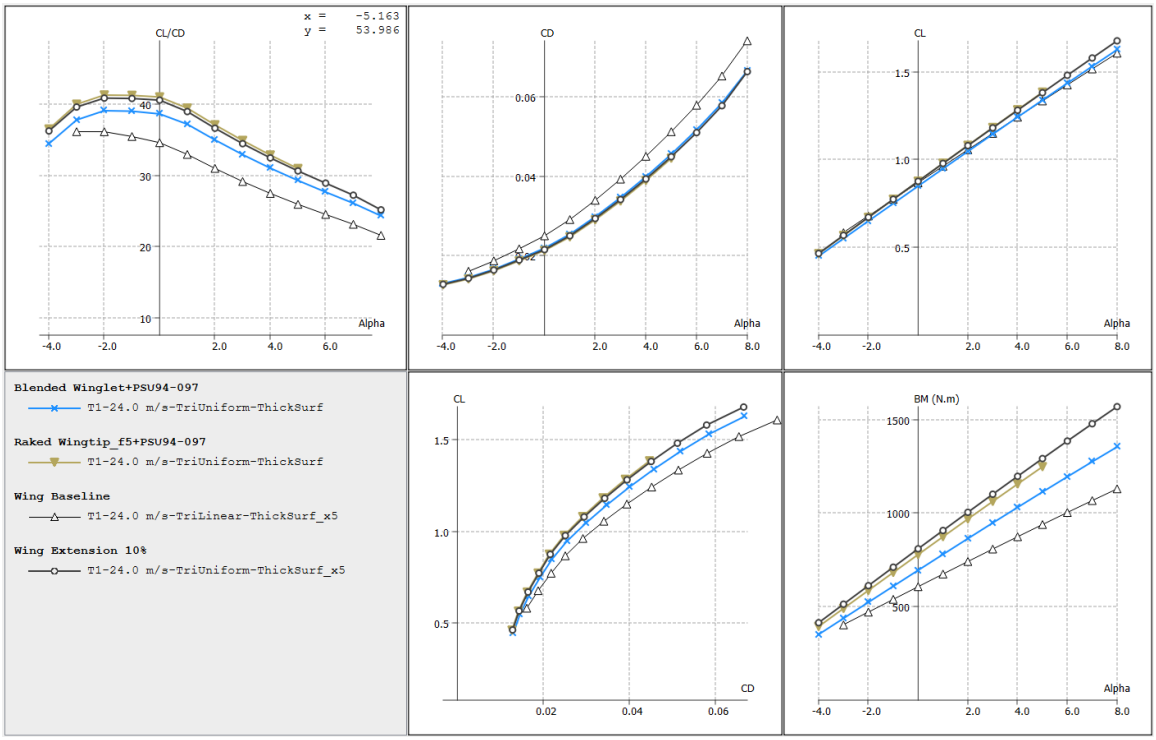

Figure 39. Aerodynamic coefficients for the four configurations of the wingtip devices: baseline geometry (a), wing extension (b), raked wingtip (c), and blended winglet (d).

These modifications are all completed in an attempt to improve the wing's performance and, ultimately, to provide an increase in airplane range and endurance. Since surveillance is the primary mission of the UAV, increasing the flying time is always desirable.

Anderson [5] analyzed the relation between the lift and drag coefficients and the thrust and power required for a level, unaccelerated flight. . The thrust required (T_R) is dependent on the airplane weight *(W)* and the L/D ratio, as given in Equation 10. From

this equation, it can be deduced that a higher L/D ratio will result in a lower required thrust, and therefore, the range of the airplane will be maximized:

$$T_R = \frac{W}{C_L / C_D} = \frac{W}{L / D}. \tag{10}$$

Although the L/D ratio is a good measure of the wing's aerodynamic efficiency, there is a similar ratio that best describes the performance when looking for improvement in the endurance of the UAV. The power required for a level unaccelerated flight is the product of the thrust required times the velocity of flight:

$$P_R = T_R * V_\infty. \tag{11}$$

It is known that lift is computed with Equation 12, where the required velocity can be computed:

$$L = W = q_\infty S C_L = \frac{1}{2} \rho_\infty V_\infty^2 S C_L \tag{12}$$

$$V_\infty = \sqrt{\frac{2W}{\rho_\infty S C_L}}. \tag{13}$$

Combining Equations 13 and 10 into Equation 11, it is found the relation of the power required with the lift and drag coefficients:

$$P_R = \frac{W}{C_L / C_D} \sqrt{\frac{2W}{\rho_\infty S C_L}} \rightarrow\rightarrow\rightarrow P_R = \sqrt{\frac{2W^3 C_D^2}{\rho_\infty S C_L^3}} \propto \frac{1}{C_L^{3/2} / C_D}. \tag{14}$$

In conclusion, to get the maximum endurance, the power required needs to be the minimum; therefore, endurance is maximized at peak values of $C_L^{3/2} / C_D$ and range is maximized for peak values of C_L/C_D. This relationship can be seen in a graph where the required power is plotted versus the flight velocity, as shown in Figure 40.

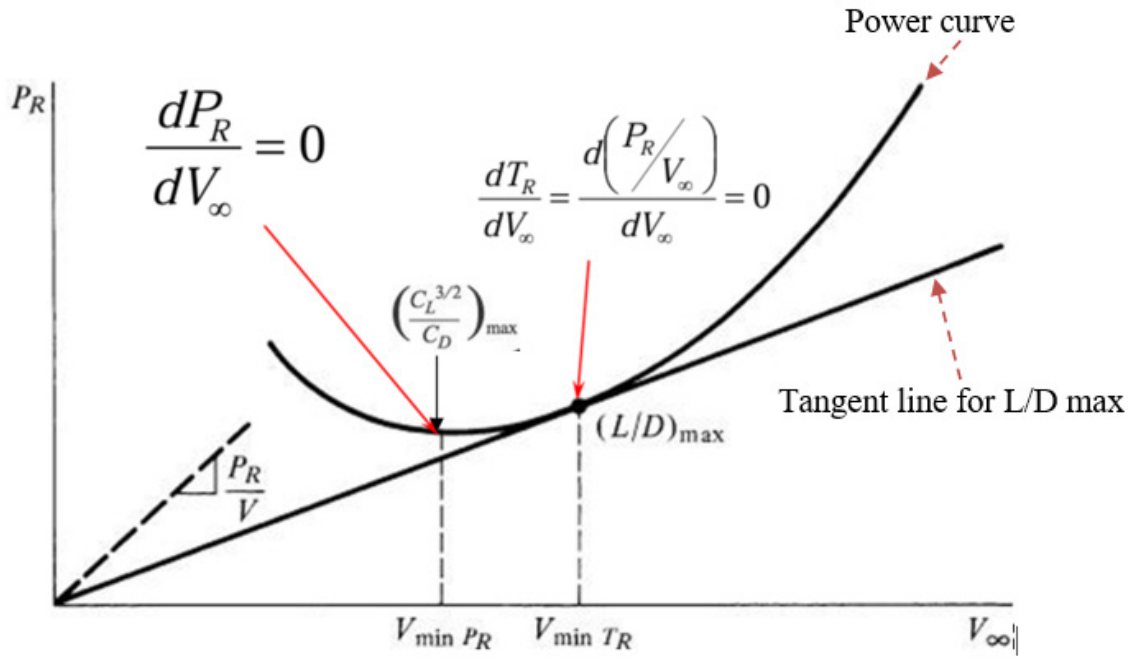

Figure 40. Power required curve. Adapted from [5].

Because the function of the UAV is more focused on surveillance missions, endurance is of greater importance than range is. The ratio of the $C_L^{3/2} / C_D$ coefficients was plotted for the four wing configurations studied. The results are presented in Figure 41. A close view of this graph suggests that a higher $C_L^{3/2} / C_D$ ratio (best endurance) is achieved at one degree of AoA, in contrast to the higher C_L / C_D ratio (best range) at a negative AoA.

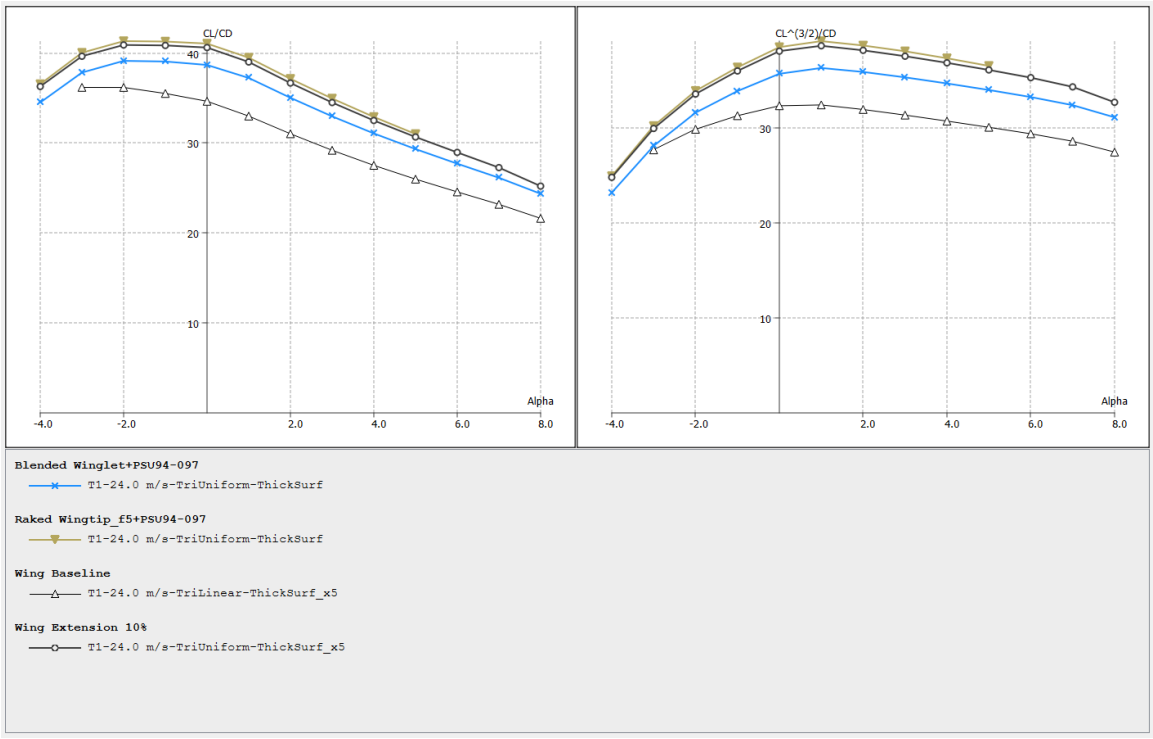

Figure 41. Plot of coefficients C_L / C_D (best range) and $C_L^{3/2} / C_D$ (best endurance) at different AoAs

VII. ANALYSIS IN CFX OF THE RESULTANT OPTIMIZED CONFIGURATIONS

Low-fidelity numerical methods are a good starting point to analyze and explore a wide variety of parameters affecting the performance of the UAV wing. From Figures 20, 21, 22, and 23 in Chapter V, the error between the low-fidelity numerical methods and the CFD analysis becomes apparent. The exploration of the whole set of parameters performed with the Flow5 software would not have been possible in the same period of time if CFX had been used. Although these low-fidelity numerical methods are not precise, they have a close relationship with data coming from CFD analysis in a fraction of time, and that was the main reason to use them as the first step in the analysis. Now, the three resultant optimized configurations are analyzed using CFX software. The results are compared with each other and taken as a reference to the values presented in Chapter V, which are the original wing configuration.

A. GEOMETRY MODIFICATION

The first step is to capture the geometry in Solidworks software to create the fluid domain to be analyzed in CFX. The resultant optimized parameters obtained in Chapter VI are used as a reference to design the final three configurations. Figures 42, 43, and 44 present the resultant final geometry and its main parameters of the wing extension, raked wingtip, and blended winglet, respectively. The original baseline configuration was presented in Figure 12.

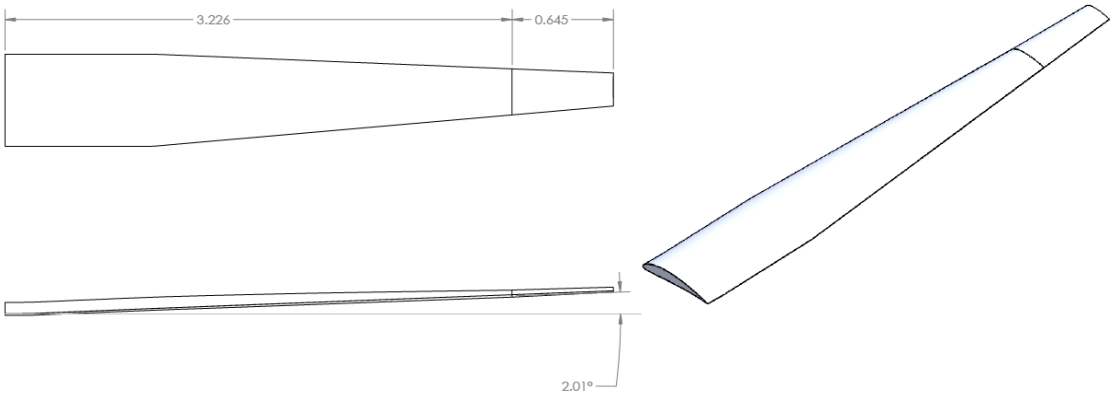

Figure 42. Half of the UAV wing with 10% wing extension. Dimensions are in meters.

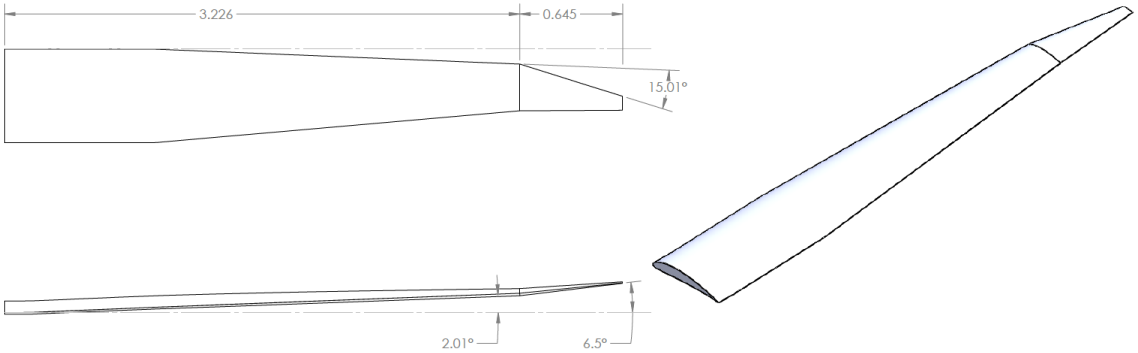

Figure 43. Half of the UAV wing with raked wingtip implemented. Dimensions are in meters.

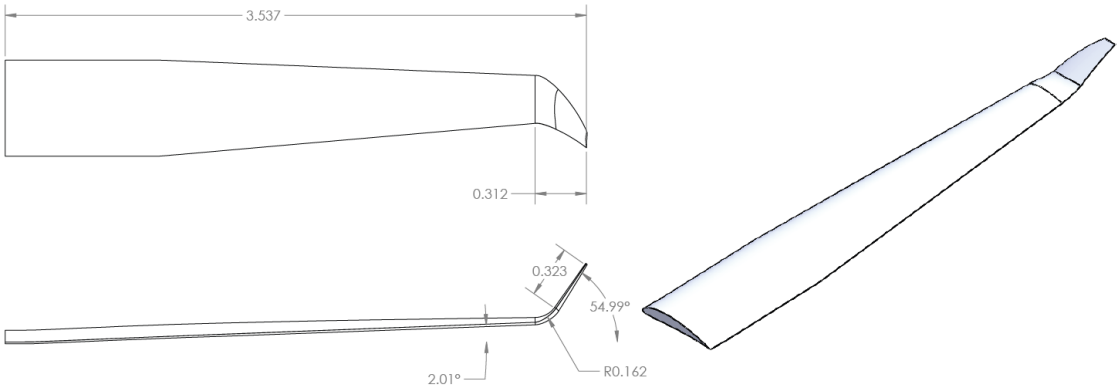

Figure 44. Half of the UAV wing with blended winglet implemented. Dimensions are in meters.

B. CFD ANALYSIS AND FINAL RESULTS

Following the same procedure described in Chapter V, Section B, the three configurations were analyzed to capture their characteristic aerodynamic coefficients. Minor mesh modifications were necessary because of the smaller curvatures on the wingtip profiles, as in the raked wingtip and blended winglets. The plots of the L/D, lift coefficient, drag coefficient, bending moment coefficient, and pitching moment coefficient are presented in Figures 45, 46, 47, 48, and 49, respectively. The reference area, MAC, and semispan were changed accordingly for each configuration when computing the individual coefficients.

The comparison of the C_l/C_d between the four wing configurations indicates that the raked wingtip is the more efficient wingtip device for the flight conditions stated. Compared to the baseline configuration, it provides a significant improvement, as depicted in Figure 45.

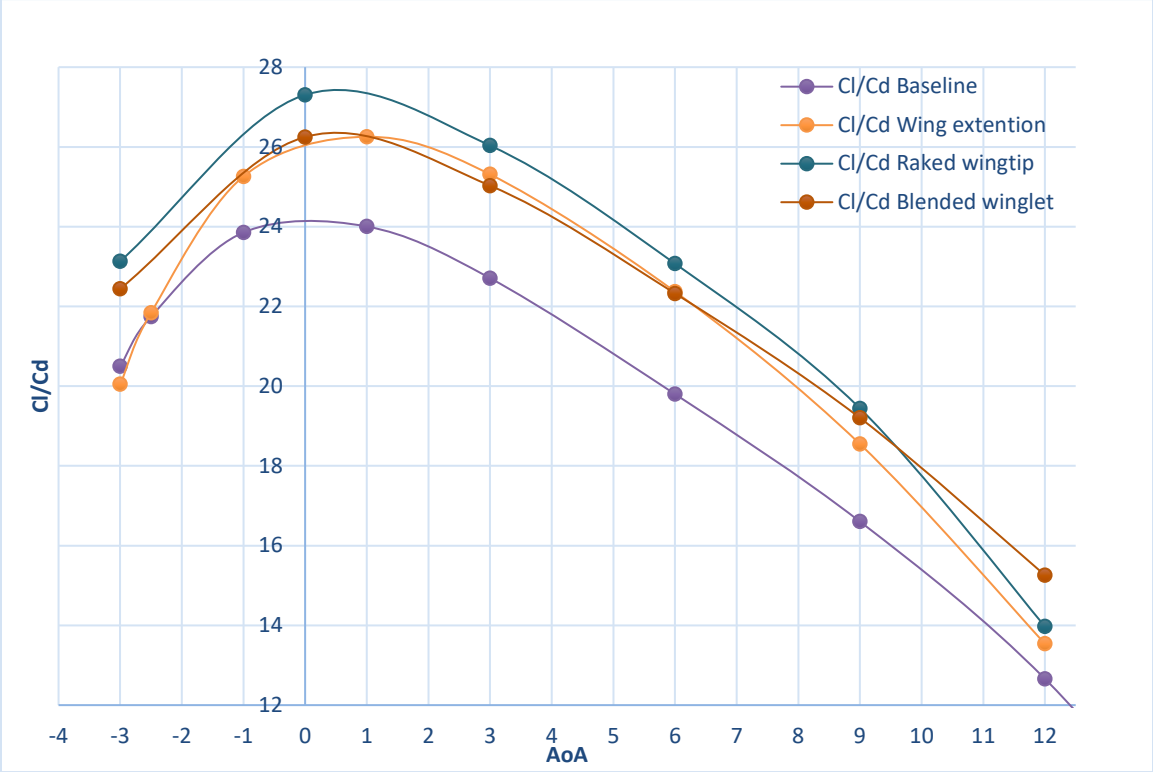

Figure 45. Comparison of the Cl/Cd coefficient for the four wing configurations analyzed

The lift coefficient is slightly higher for the raked wingtip at a small AoA, as can be seen in Figure 46. Blended winglets result in higher Cl at a high AoA. The drag coefficient is presented in Figure 47, where the difference is noticeable compared to the baseline configuration, and the raked wingtip results in the lowest Cd. Drag reduction is even larger at a high AoA, for example when the UAV is climbing, since the induced drag is higher in this flight condition. To better notice this difference, only the pressure drag is plotted in Figure 48, where the raked wingtip and blended winglet have similar values and are both lower than the wing extension values. The reduction in the induced drag is the main contributor to the higher C_l/C_d ratio.

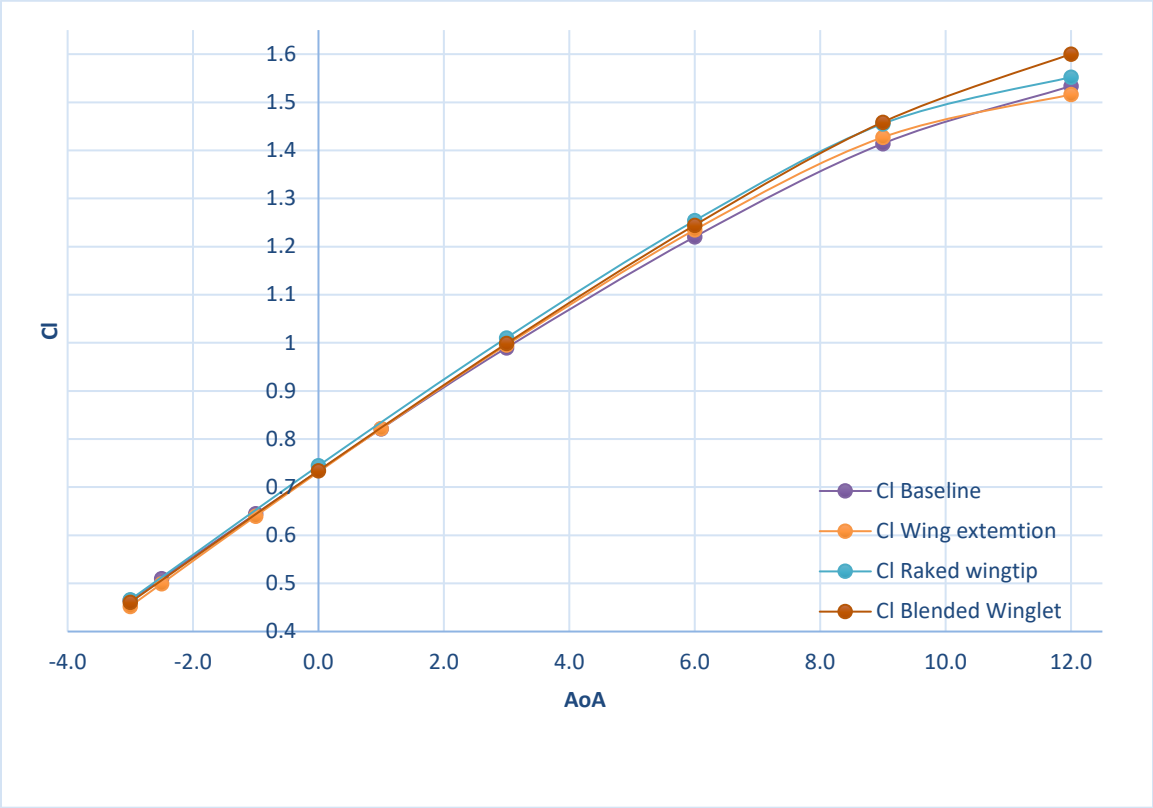

Figure 46. Comparison of the lift coefficient for the four wing configurations analyzed

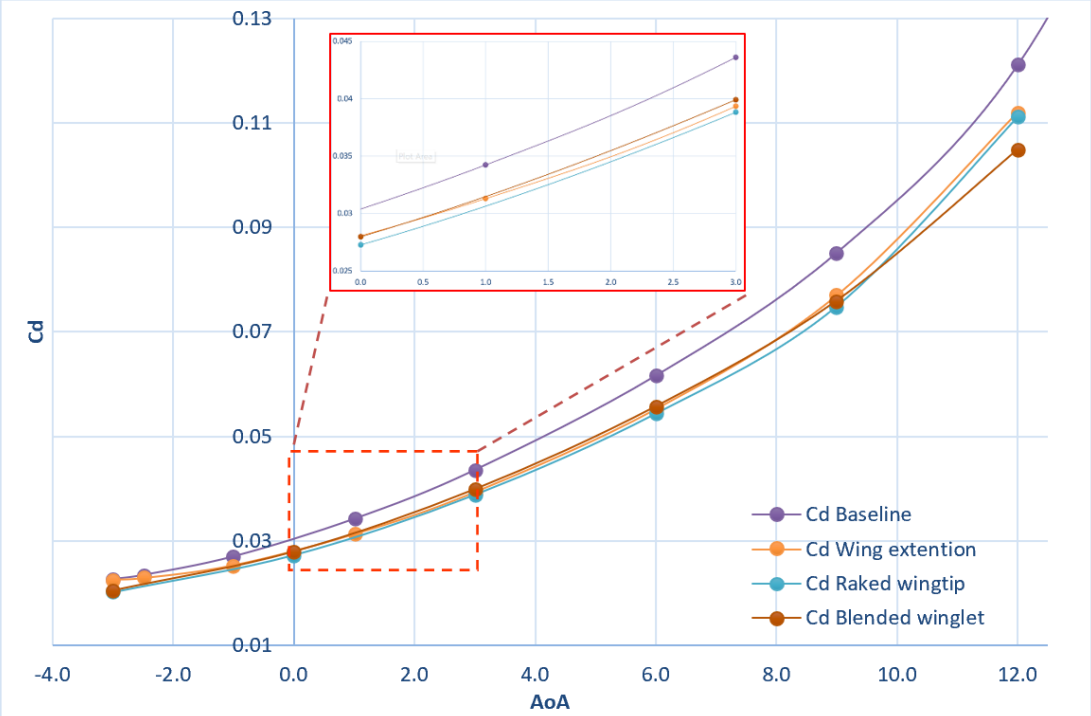

Figure 47. Comparison of the drag coefficient for the four wing configurations analyzed

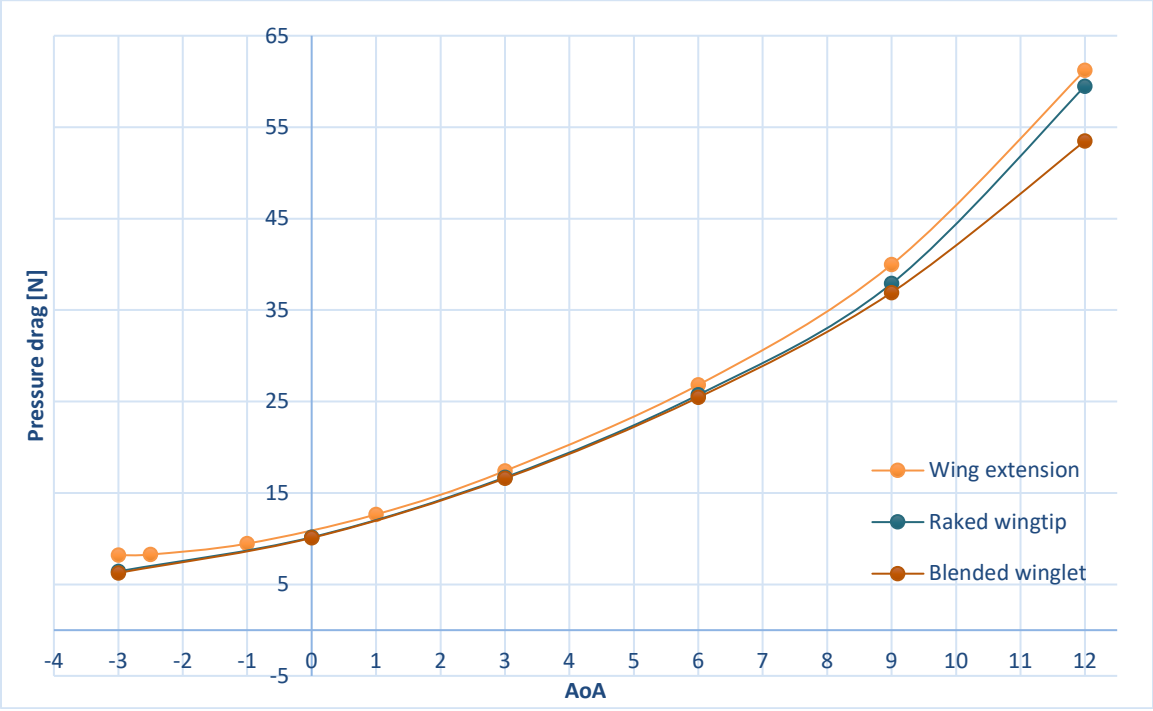

Figure 48. Pressure drag for the four wing configurations analyzed

The bending moment is similar for the raked wingtip and wing extension, but higher than the baseline configuration mainly because of the increment in wingspan and planform area. At a high AoA, the blended winglet develops an even larger bending moment than the other configurations tested due to the high lift coefficient at these angles. Lowering the bending moment reduces the requirement for structural reinforcement of the wing and therefore minimizes additional structural weight. Because this is a small aircraft, the aerodynamic performance is more critical than the structural weight is, as stated by Drela et al. [10]. The bending moment plot is presented in Figure 49.

Finally, regarding the pitching moment coefficient, the raked wingtip results with the lowest, but in general this coefficient remains similar than the original configuration for all the modifications tested, as depicted in Figure 50. This effect is desirable because no additional tuning will be needed to stabilize the airplane.

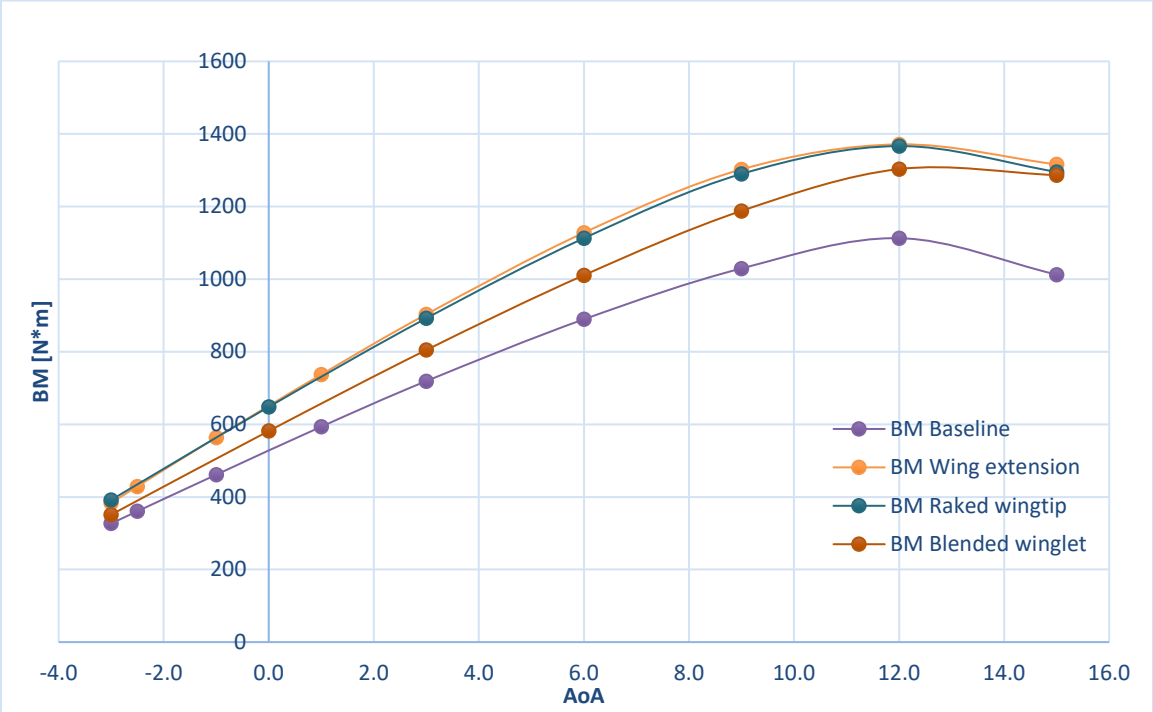

Figure 49. Comparison of the bending moment for the four wing configurations analyzed

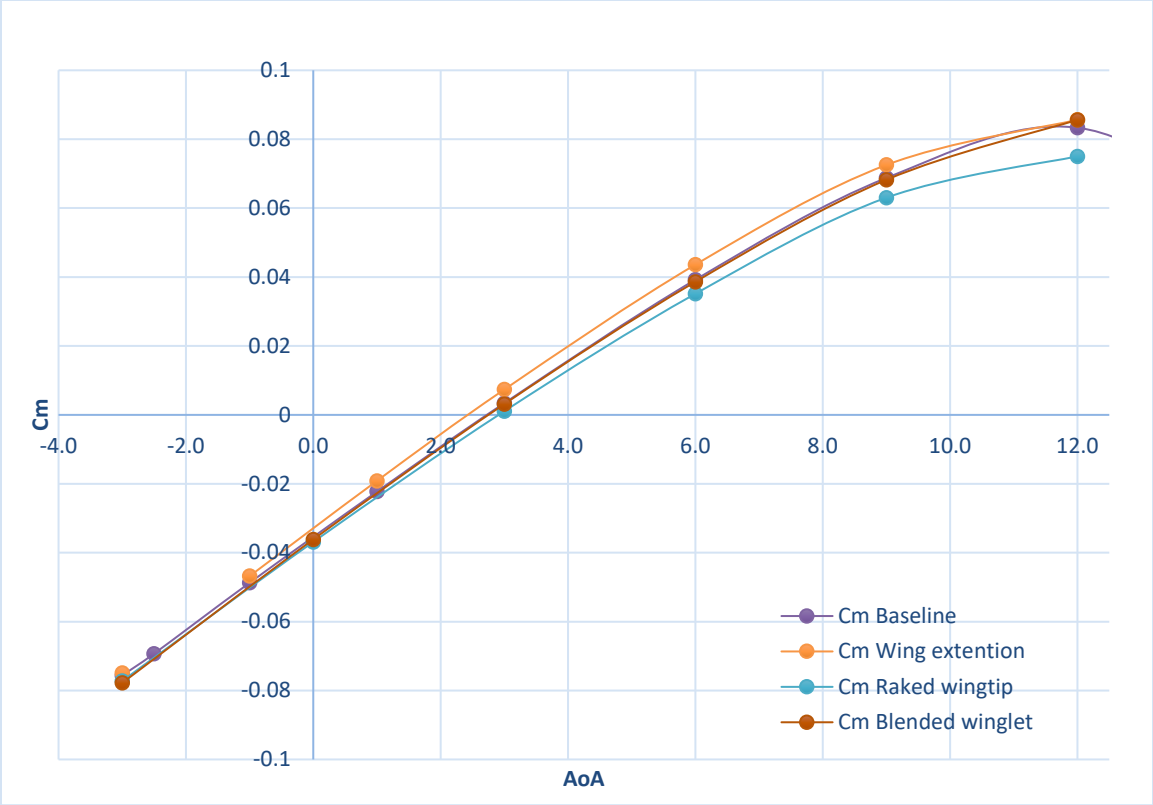

Figure 50. Comparison of the pitching moment coefficient for the four wing configurations analyzed

The endurance of an airplane is directly related to the power required for a steady, unaccelerated flight. Equation 14 states that the power required is inversely proportional to the $C_L^{3/2} / C_D$ ratio. Therefore, to minimize the power required and extend endurance, the $C_L^{3/2} / C_D$ ratio needs to be the maximum, as depicted in Figure 40, in the power required curve. The behavior of the $C_L^{3/2} / C_D$ ratio is presented in Figure 51, as a function of AoA. Analyzing this plot, I can state that for this flight condition, 24 m/s velocity, the maximum endurance is reached when the UAV operates between 2 to 4 AoA, and from Figure 45, the maximum range requires between 0 to 1 AoA. This trend is comparable with the results obtained from the Flow5 software, presented in Figure 41. The blended winglets appear to perform better at a higher AoA but are not an ideal solution for a UAV flying under cruise conditions.

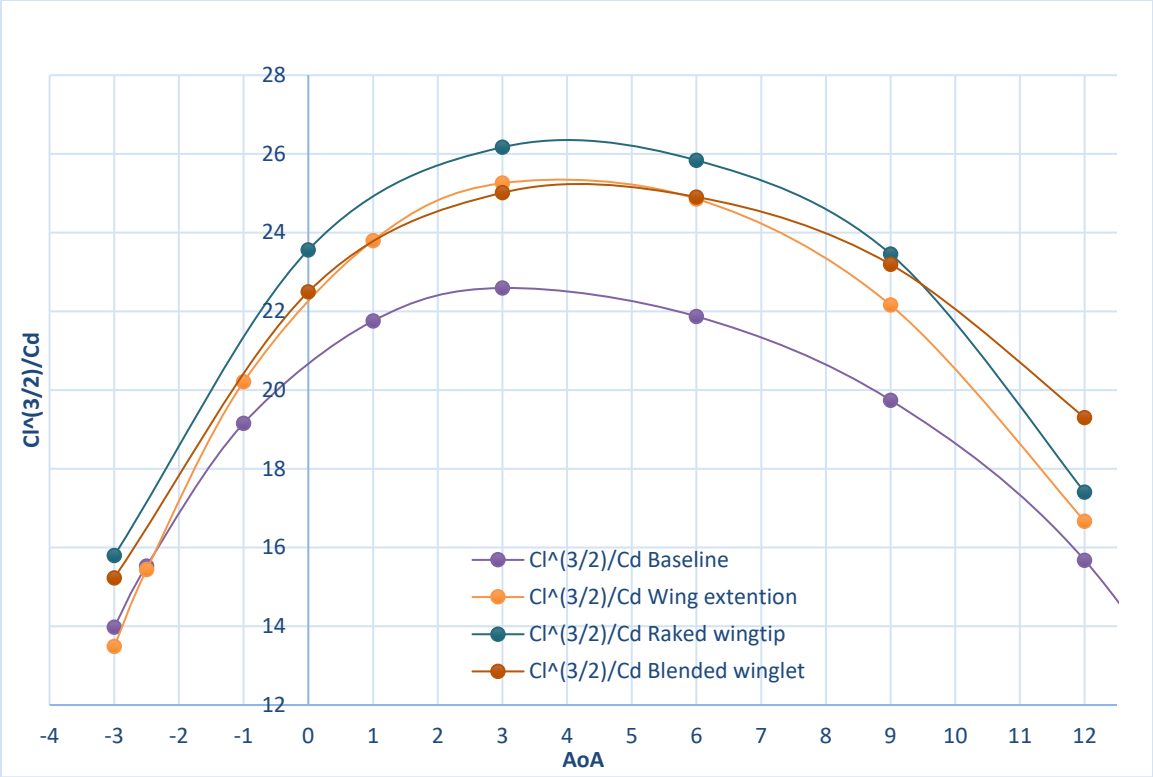

Figure 51. Comparison of the $C_L^{3/2} / C_D$ ratio for the four wing configurations analyzed

C. RANGE AND ENDURANCE CALCULATIONS

To have an idea of how much improvement is achieved by the addition of the raked wingtip to the wing, the calculation of range and endurance is performed. The Breguet equations for range and endurance are used to compute these parameters. The range under cruise conditions are given by Equation 15, and the endurance under cruise conditions is given by Equation 16:

$$R = \frac{\eta_{p,\,\text{cruise}}}{c_{\text{bhp,cruise}}} \left(\frac{L}{D}\right)_{\text{cruise}} \ln\left(\frac{W_1}{W_2}\right) \tag{15}$$

$$E = \frac{\eta_{p,\,\text{loiter}}}{c_{bhp,\,\text{loiter}}} \sqrt{2\rho_\infty S} \left(\frac{C_L^{3/2}}{C_D}\right)_{\text{loiter}} \left(W_2^{-1/2} - W_1^{-1/2}\right), \tag{16}$$

where η_p is the propeller efficiency, c_{bhp} is the engine specific fuel consumption, W_1 and W_2 correspond to the initial and final weights of the aircraft for the flying segment, ρ_∞ is the freestream air density, and S is the planform area of the wing.

The average propeller efficiency ranges between 0.6 and 0.8, according to Raymer [6]. The value of 0.7 is used for this calculation. The engine-specific fuel consumption was taken from the manufacturer's data sheet. The maximum take-off weight of the UAV is 96 kg, and the fuel capacity is 16 kg. The air density was set to 1.112 kg/m^3 computed at 1000 m altitude, where the UAV operates during the surveillance mission. According to Panagiotou et al. [39], for a medium-altitude, long-endurance UAV, the contribution of the wing to the total drag of the airplane ranges between 30% and 70% for different flight conditions, and 40% corresponds to loiter conditions. To develop this calculation only for comparative purposes, a 60% drag is added to the calculated wing drag to represent the UAV total drag. The estimated range and endurance are presented in Table 8.

Table 8. Range and endurance calculations for the baseline and raked wingtip configurations

Configuration	$(C_L)_{\text{loiter}}$	$(C_D)_{\text{loiter}}$	$\left(\frac{L}{D}\right)_{\text{cruise}}$	S (m^2)	Range (km)	Endurance (hours)
Raked wingtip	1.0105	0.0621	27.5	3.358	631.74	16.93
Baseline	0.9898	0.0697	24	3.10	551.34	14.04

Even though the calculations presented in Table 8 are not precise because the estimation of the total drag is approximate at best, the increment in range and endurance are significant with the new configuration. The analysis of the complete UAV to capture the correct lift and drag is the next step to focus on in this analysis.

THIS PAGE INTENTIONALLY LEFT BLANK

VIII. CONCLUSIONS AND FUTURE WORK

This thesis developed the numerical simulations of a UAV wing while searching for improved aerodynamic performance by implementing minor modifications to the wing, isolated to the wing tip. The modifications explored included a wing extension, a raked wingtip, and a blended winglet. Taking advantage of low-fidelity numerical tools like the Flow5 software, the optimum shape of the proposed configuration was found. The preliminary results from this software suggest that improvement can be achieved with all the modifications proposed, but the raked wingtip results in the best option for the established flight conditions.

The optimized configurations were analyzed using ANSYS-CFX to properly capture the viscous effects and boundary layer behavior, which are limitations of the low-fidelity tool used. A comparison of the results from both numerical schemes indicates that there is a decent relationship between them and suggests an efficient way to analyze and explore different configurations during the preliminary design.

Raked wingtips appear to be the best option to implement on the UAV wing to enhance both its range and endurance with a minor increase in the wing bending moment and practically no change to the pitching moment. Analytical estimation of the additional drag was done to estimate the range and endurance for the original baseline and the optimized raked wingtip configuration. The results indicate that there is an increase of about 20% in the endurance and 14% in the range. I am aware that this result is optimistic; nevertheless, it is an indication of possible improvements in the UAV performance.

Future work consists precisely of analyzing the whole airplane to obtain more realistic numbers about the improvement reflected in the UAV's range and endurance. Because only minor changes to the wing were allowed, resulting in only a small part of the wing being optimized, the increase in aerodynamic performance is limited. An additional step in the search for improvement would be the complete redesign of the wing using the methodology and tools presented in this thesis. The time, computational

resources, and complexity will be significant, but the performance of the airplane can be optimized in more than one area.

Finally, according to Makgantai et al. [43], Gurney flaps, morphing winglets, and adaptive winglets are considered state-of-the-art to maximize the performance of an aircraft, including a UAV.

APPENDIX A. CREATING AND ANALYZING WINGS IN FLOW 5

The Flow5 software is a potential-flow solver that incorporates the fundamental functionalities of Xflr5 while also introducing new features to enhance its user-friendliness, versatility, and precision. There is one functionality available on Xflr5 that is not present on Flow5: the Xfoil's direct and inverse analysis. To analyze the airfoils and have the 2D viscous data, Flow5 software can interchange information with Xflr5. The software is available to download at [25].

A. ANALYZING FOILS IN FLOW5

The analysis starts by loading or creating the airfoils in Flow5. There are different ways to load or create an airfoil, which start by accessing the **Foil** menu and then **Design**:

- NACA foils; enter only the four or five digits defining the NACA foil geometry
- from coordinates
- from spline
- from camber and thickness: manually drag the control points defining the geometry changing these parameters
- interpolate two existing airfoils; choose the airfoils to interpolate and define what percentage of each one to interpolate
- open a airfoilname.dat file with the coordinates of the airfoil

Once the airfoil is loaded in Flow5, the airfoil needs to be exported to Xflr5 by pressing the blue export button, shown in Figure 52. This action will open Xflr5 software and temporarily load the airfoils to perform the analysis.

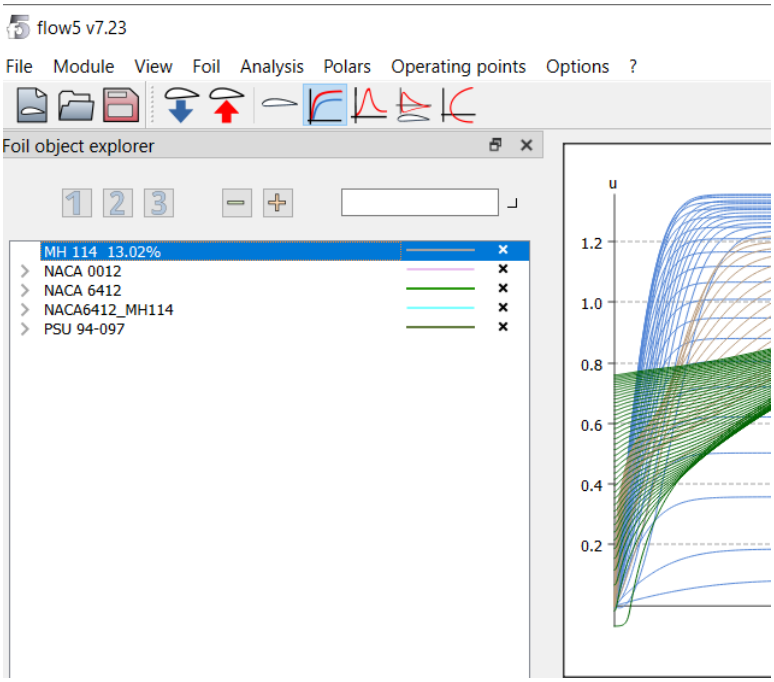

Figure 52. Exporting (blue arrow) and importing (red arrow) icons from Flow5 to analyze the airfoils in Xflr5

Once inside Xflr5, from the **Analysis** menu, choose **Batch analysis** and then T1 type to define a range of Reynolds number and AoA range analysis, as specified in Figure 53. The Reynolds number needs to cover from the lowest (tip airfoil) to the largest (root airfoil) numbers. To perform the analysis, hit the **Analyze** button, as shown in Figure 53. This action will generate all of the polars of the airfoil analyzed and presented, as depicted in Figure 54. The parameters plotted on each graph can be changed by double-clicking on the graph. Since Xflr5 is opened from Flow5, this data is stored in a temporary folder. At this point, it is only necessary to hit the **Save** button and exit from Xflr5.

Back in Flow5, hit the import airfoil data (red arrow), presented in Figure 52, to load the data generated inside Xflr5. Now the 2D airfoil data is available to use and process inside of Flow5.

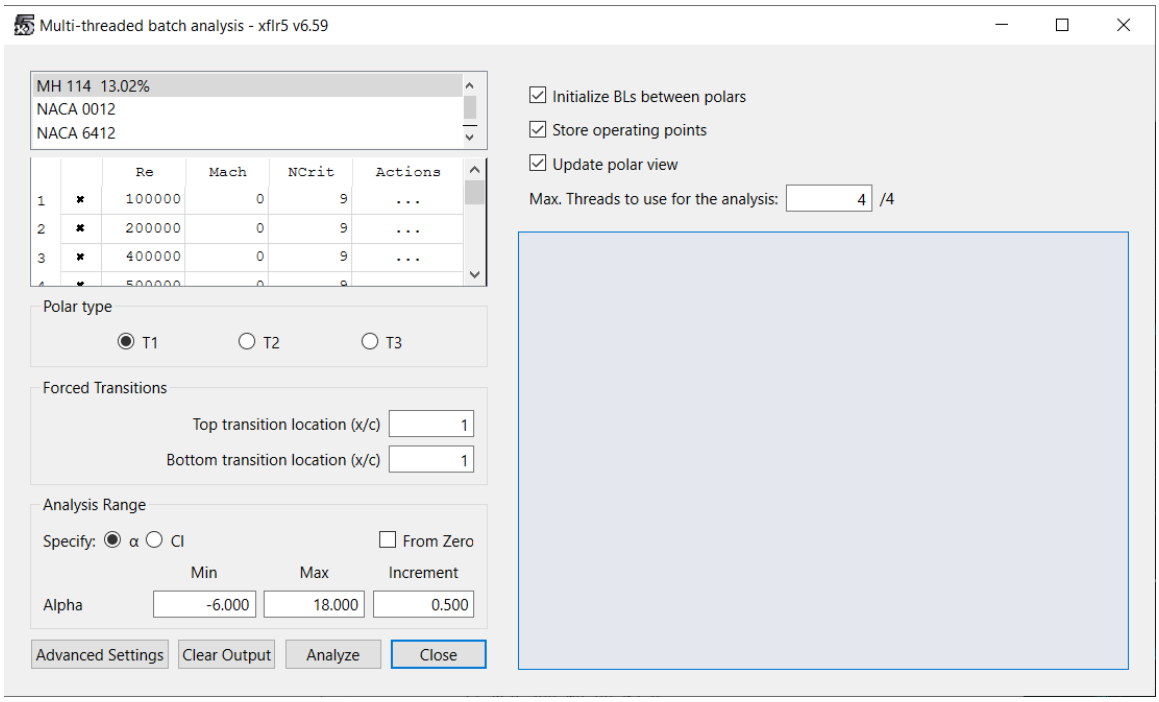

Figure 53. Batch analysis definition by setting the Reynolds number range and AoA range

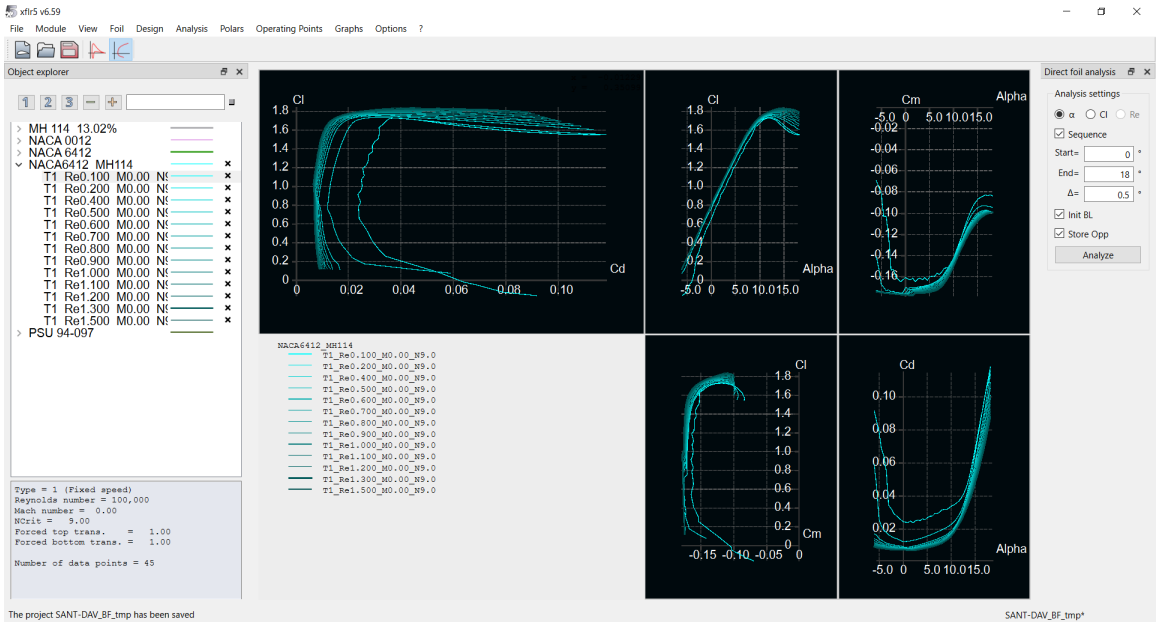

Figure 54. Airfoil batch analysis results plotted in Xflr5

B. CREATING WING GEOMETRY IN FLOW5

With the 2D airfoil data available in Flow5, the plane geometry can be created; in this case, only the wing is created.

- Choose **Module** menu and then **Plane design**.

- From the **Plane** menu, choose **Define a new plane**. This action will open a template with some preloaded geometry. Three surfaces are available to select: main wing, elevator, and fin. Because only the wing will be analyzed, remove the elevator and fin from the template by hitting the three dots under the Action option, as shown in Figure 55. Change the name of the airplane and, finally, save the changes and exit. This will create a flat geometry of the wing with random parameters.

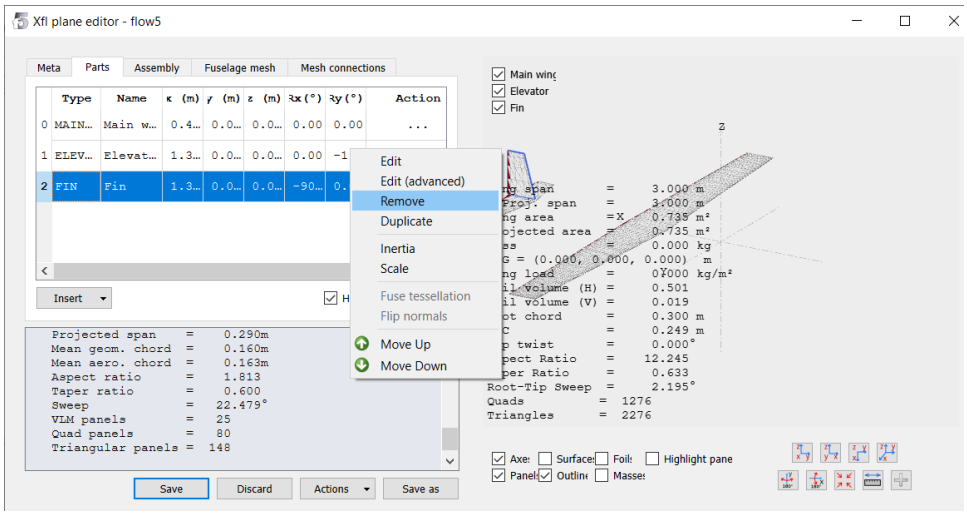

Figure 55. Plane editor interface to select the surfaces to be analyzed

- To modify the wing geometry, hit the **Plane** menu, then **Active plane**; select **Wing** and **Edit**. This will open the wind editor interface, where the complete wing geometry can be set, as shown in Figure 56. The wings can have more than one section, and each section can be defined individually. The main parameters needed to define each wing section are the y-

position, chord, offset (distance measured from the leading-edge root airfoil to the leading-edge section airfoil to be defined; this is the way that Flow5 sets the sweep angle), dihedral, twist, airfoil, and the number of panels for each section.

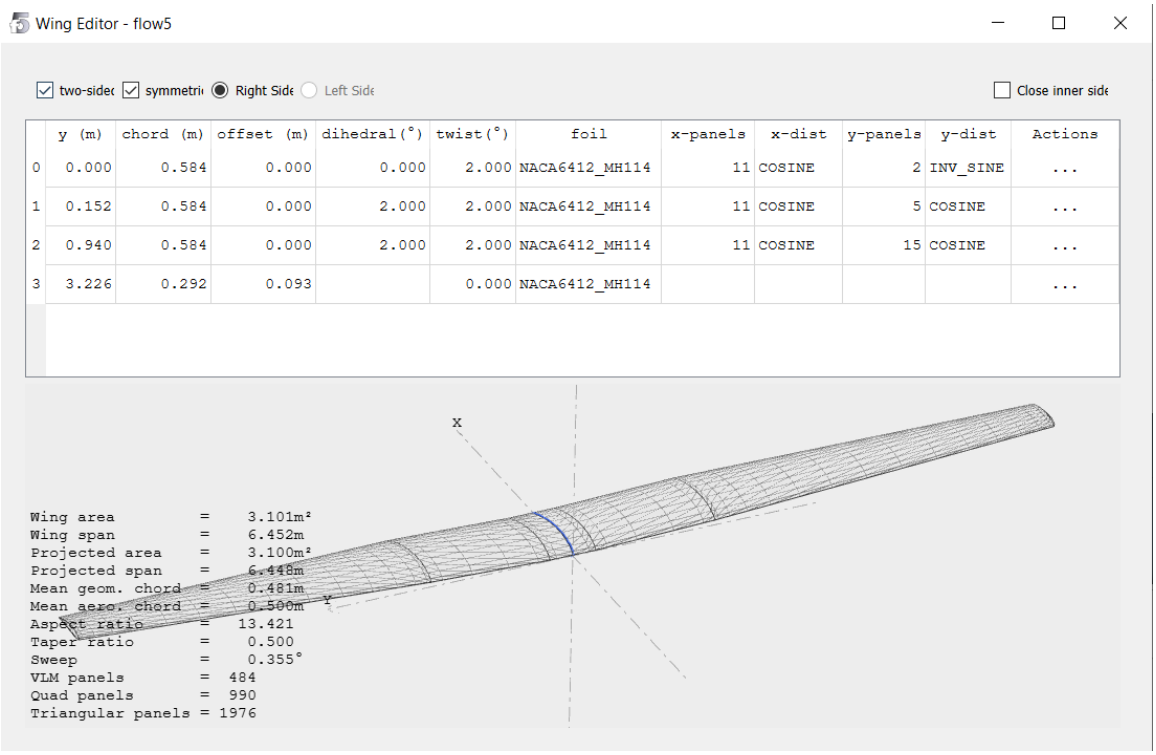

Figure 56. Wing editor interface to set the wing parameters

C. ANALYZING WINGS IN FLOW5

Once the wing geometry is created in Flow5, the type of analysis needs to be defined. With the wing geometry open, select **Define an analysis** from the **Analysis** menu. This will open the analysis definition interface shown in Figure 57. Choose the options that best fit the analysis. For example, the wing analyzed was set with the following options:

- **Polar type**. There are eight types of polar from which to choose; detailed information of each one is available on the software website. In this case, I

am interested in analyzing the wing at a specific velocity; therefore, Type 1 (fixed velocity) is chosen, and the velocity is set to 24 m/s.

- **Method**. The are six analysis methods available, two VLMs, one LLT, and three panel methods (uniform density quad panels, uniform density triangular panels, and linear density triangular panels). Also, this window allows the user to select to model a thin or thick surface. All the analysis methods were tested and compared with data from CFX, and the uniform density triangular panels proved to be the more confident option to select.

- **Viscosity**. The viscosity effect can be activated or deactivated from the analysis. Normally, the viscous effects are underestimated with this low-fidelity numerical analysis.

- **Inertia**. The inertia can be taken from the information available from the complete airplane or set individually. Enter the plane mass and center of gravity location if required.

- **Reference dimensions**. Choose from wing planform, wing planform projected on xy-plane, or enter a custom value.

- **Fluid**. Enter the fluid density and kinematic viscosity values or select the altitude and temperature to automatically load its values.

- Save changes and exit.

- Finally, define the minimum, maximum, and the step of the AoA to be analyzed, and hit the **Analyze** button.

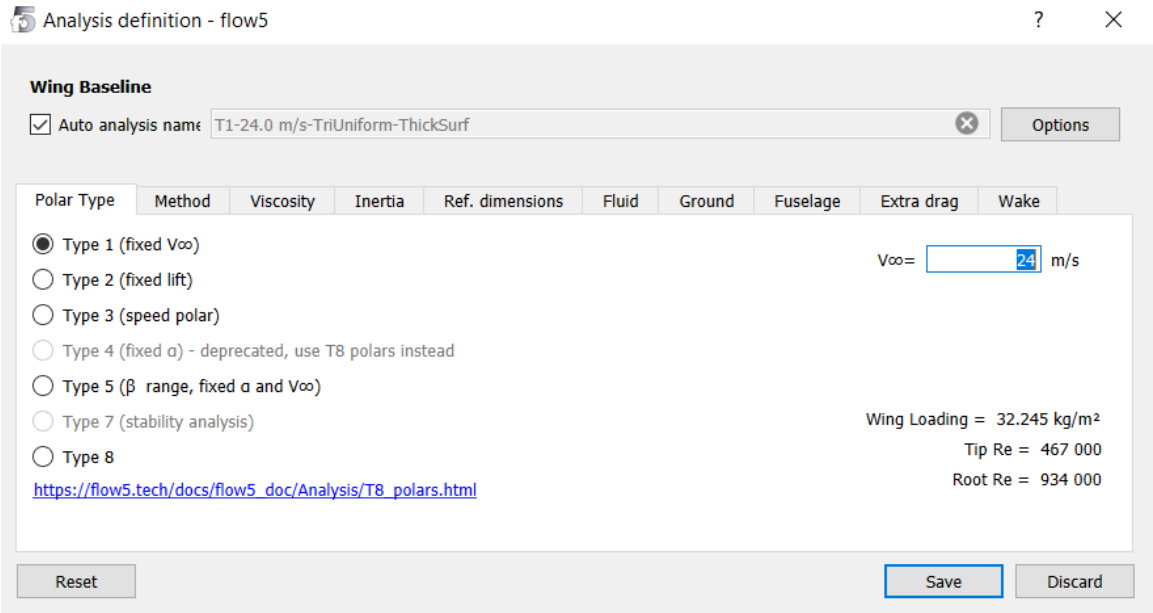

Figure 57. Analysis definition interface

The simulation will run for some seconds, and the results will be available to visualize on the polar view. Like airfoil analysis, the more characteristic coefficient plots are presented, but it can be chosen from a wide range of parameters to plot.

The wing or complete airplane can be duplicated to modify its geometry and compare the resultant polars, as depicted in Figure 58. Additionally, external polars can be imported to compare with the data generated in this software. To import external data, from the **Polar** menu, choose **Import external polar**. The polar data points interface will ask for the values for the desired parameters. Select the parameters to import and only copy and paste the information in this area. The data is now available to visualize and compare with the previous data generated.

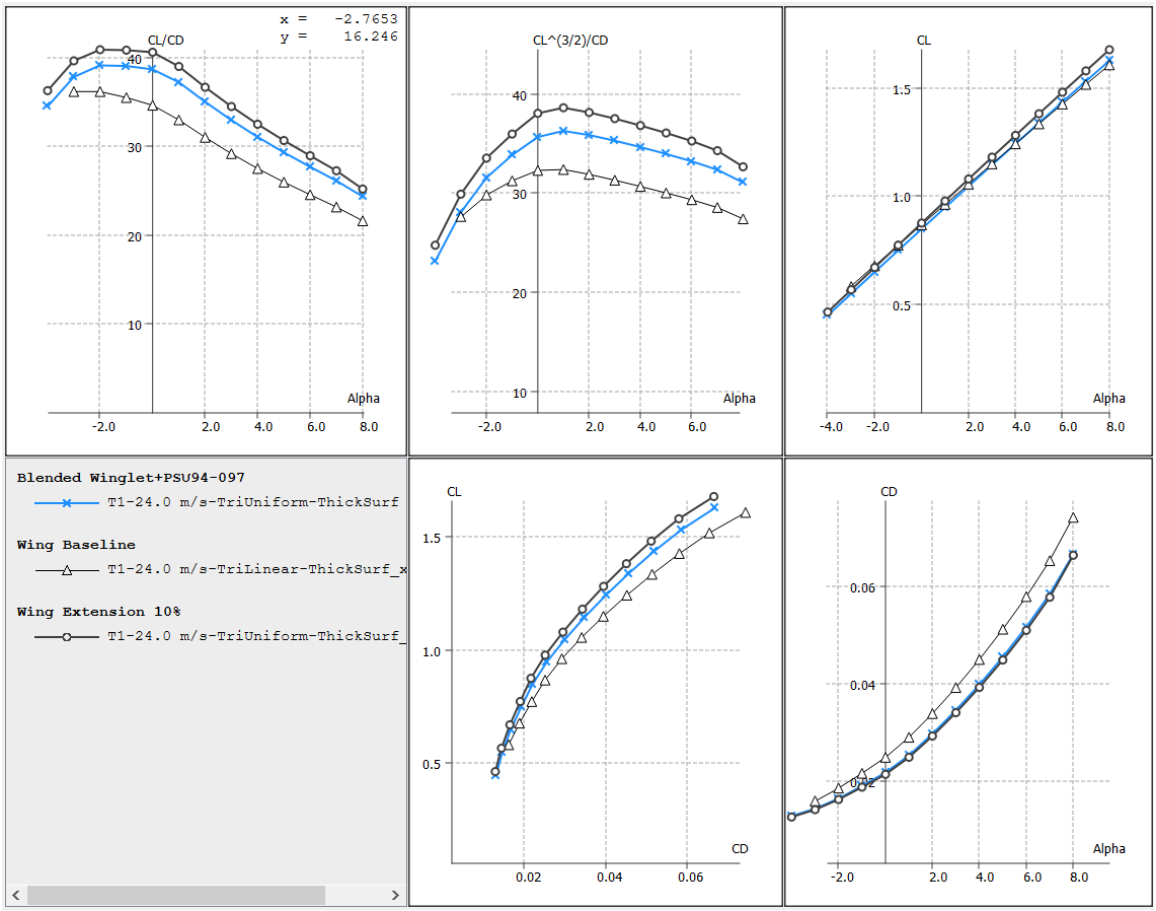

Figure 58. Polar view after analysis is completed

APPENDIX B. OPTIMIZATION PROCESS IN FLOW 5

Flow5 has an optimization feature that is capable of exploring different variables while searching to reach an objective or multiple objectives. For example, the user can explore modifying the wing parameters shown in Figure 56 to maximize *Cl/Cd* and minimize *Cm*. Flow5 used the MOPSO algorithm to perform the optimization process, which is described on the software website [36]. To access the optimization module, select the wing or plane, then from the **Plane** menu, choose **Active plane** and then **Optimize**. This action will open the Optimization 3d interface presented in Figure 59, where the list of planes will be displayed to choose from.

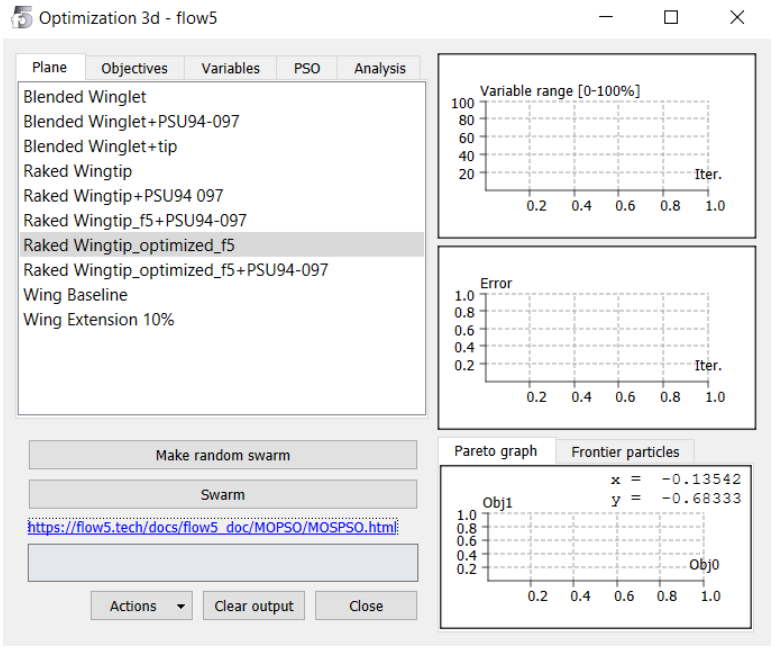

Figure 59. Optimization 3d interface of Flow5 software

To set the optimization process, follow these steps:

- **Plane menu**: Select the plane to optimize from the list available if there is more than one configuration displayed.

- **Objectives menu**: Choose one of the five preloaded objectives: *Cl, Cd, Cl/Cd, $Cl^{3/2}/Cd$*, and *Cm*. There is not an option to maximize or minimize these objectives, but instead, the user can define a target value higher or lower enough for the software to try to reach.

- **Variables menu**: Select a variable to explore. There are plane variables like AoA, mass, and center of gravity location, but there are also wing variables to explore while defining the minimum and maximum values. For each wing section, the user can define the range of values to explore for the y-position (wing semispan), chord, offset, and twist.

- **PSO menu**: Choose parameters to modify. There are a set of parameters that define the PSO analysis, as shown in Figure 60. The author of the software recommends leaving the default values for the inertia weight, cognitive weight, social weight, and regeneration probability parameters since they have resulted as the best combination for the software to work properly. The only parameters that one can attempt to modify are the swarm size and maximum iterations.

- **Analysis menu**: Define the required analysis as stated in Section C of Appendix A. Since this optimization process will run hundreds of iterations, only Type 1 and Type 2 polars are recommended, as is the uniform density quad panels method. The use of thin surfaces instead of thick surfaces is also recommended. Enabling or disabling the viscous analysis will also impact the time of process required.

- Once the parameters are defined, hit the **Make random swarm** button once all these parameters have been defined. The software will create the number of particles defined as the swarm size with a combination of the values defined for each variable.

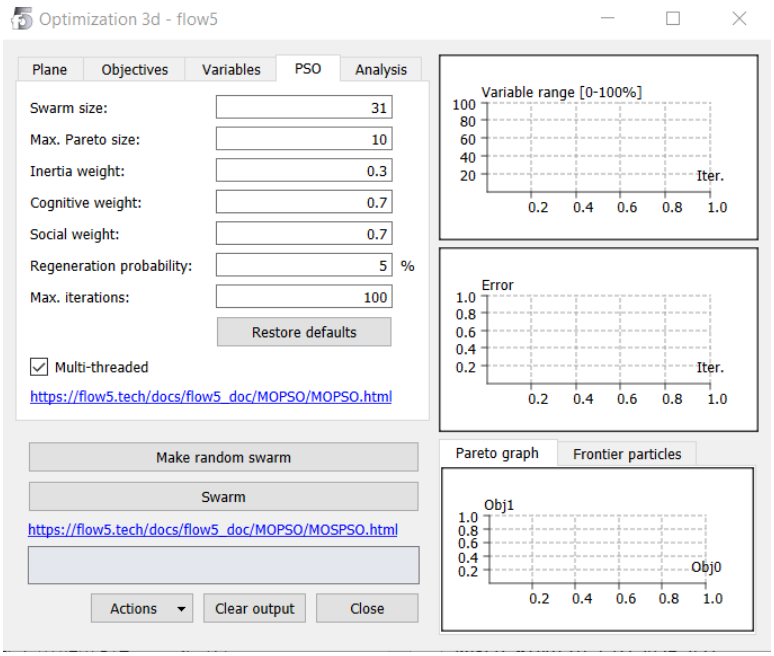

Figure 60. PSO parameters of optimization 3d interface

- Finally, hit the **Swarm** button to run the MOPSO algorithm and start the optimization process. While the process is running, one can visualize how the values of the variables are changing and affecting the objectives. Besides that, the Pareto frontier is updated dynamically after each iteration. When the process is finished, the resultant particle, which is the combination of variables that best reaches the objectives, is displayed, as depicted in Figure 61. Normally, one particle is the winner, but sometimes there is more than one particle that delivers promising results. In that case, hit the **Swarm** button again, and the software will continue refining the results, or one can explore manually the winning particles to choose the more convenient.

- If the parameters of the objectives, variables, or analysis are changed, create the initial swarm again by pressing the **Make random swarm** button and repeating the previously described process.

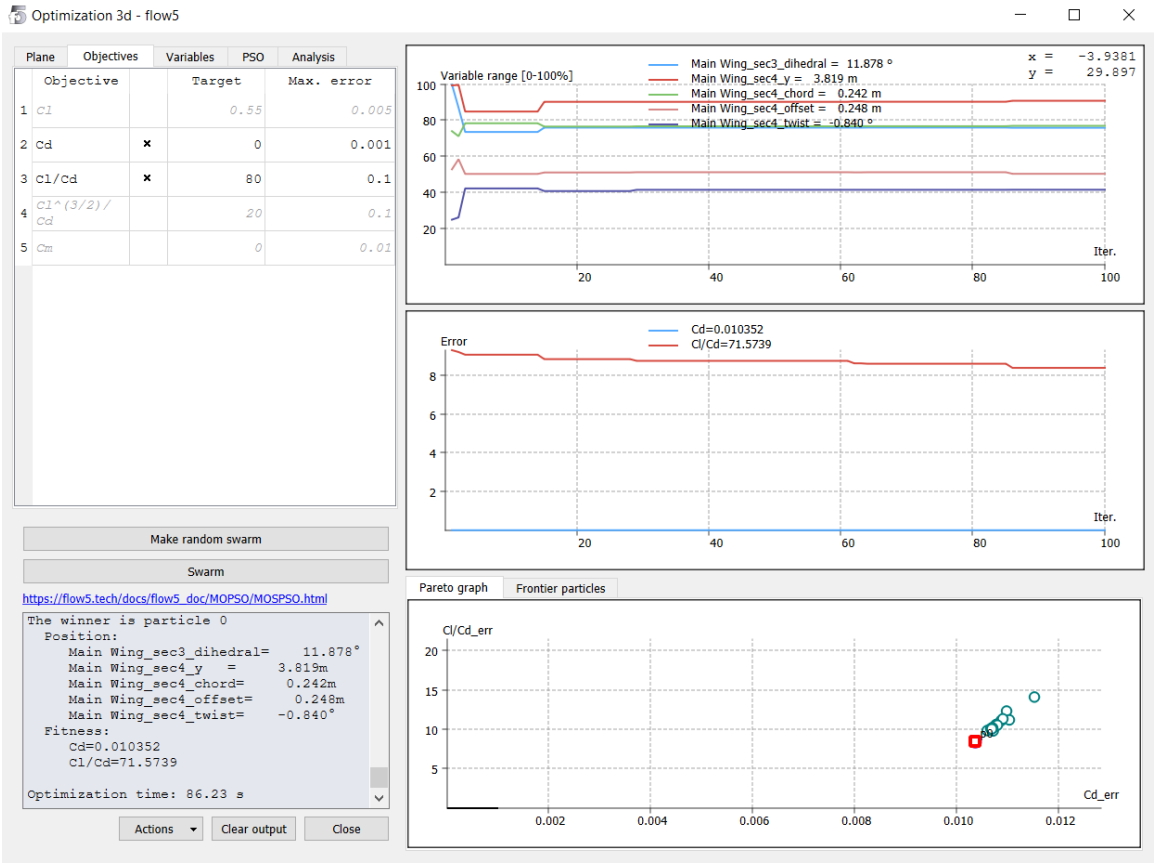

Figure 61. Optimization results

- Save the resultant optimized configuration by pressing the three dots icon and selecting **Store plane** under the Action column in the Frontier particles section. Define the name for this new configuration, which will be charged to the planes list in the main interface. This new configuration is now available to analyze, as stated in Section C of Appendix A, and compare with the unoptimized configuration.

LIST OF REFERENCES

[1] I. Kroo, "Drag due to lift: Concepts for prediction and reduction," *Annual Review Fluid Mechanics*, vol. 33, pp. 587–617, 2001.

[2] C. W. Boppe, "Aircraft drag analysis methods," AGARD, Neuilly Sur, Seine, France, 783, May 1991.

[3] E. Torenbeek, *Advanced Aircraft Design: Conceptual Design, Analysis, and Optimization of Subsonic Civil Airplanes.* in Aerospace Series. Chichester, West Sussex, U.K: Wiley, 2013. doi: 10.1002/9781118568101.

[4] D. McLean, "Wingtip devices: What they do and how they do," presented at the *Boeing Performance and Flight Operations Engineering Conf.*, Seattle, WA, EE. UU., 2005.

[5] J. D. Anderson, Jr., *Introduction to Flight*. Ney York, NY, USA: McGraw Hill, 2005.

[6] D. Raymer, *Aircraft Design: A Conceptual Approach*, 6th ed. Washington, D.C., USA: AIAA, 2018.

[7] M. H. Sadraey, *Aircraft Performance: An Engineering Approach*, 2nd ed. Boca Raton, FL, USA: CRC Press, 2023.

[8] I. Kroo, "Non-planar wing concepts for increased aircraft efficiency," presented at the *VKI Lecture Series on Innovative Configurations and Advanced Concepts for Future Civil Aircraft*, Stanford, CA, USA, Jun. 2005.

[9] J. J. Bertin and R. M. Cummings, *Aerodynamics for Engineers*, 6th ed. Boston, MA, USA: Pearson, 2014.

[10] M. Drela, J. Protz, and A. Epstein, "The role of size in the future of aeronautics," in *AIAA International Air and Space Symposium and Exposition: The Next 100 Years*, Jun. 2003.

[11] P. Mamla and C. Galinski, "Basic induced drag study of the joined-wing aircraft," *Journal of Aircraft*, vol. 46, no. 4, pp. 1438–1440, Jul. 2009.

[12] R. T. Whitcomb, "A design approach and selected wind tunnel results at high subsonic speeds for wing-tip mounted winglets," Hampton, VA, USA, Rep. NASA TN D-8260, Jul. 1976.

[13] M. D. Maughmer, "Design of winglets for high-performance sailplanes," *Journal of Aircraft*, vol. 40, no. 6, pp. 1099–1106, Dec. 2003.

[14] J. E. Guerrero, M. Sanguineti, and K. Wittkowski, “Variable cant angle winglets for improvement of aircraft flight performance,” *Meccanica*, vol. 55, no. 10, pp. 1917–1947, Sep. 2020.

[15] B. Makgantai, N. Subaschandar, and R. S. Jamisola, “Design optimization of wingtip devices to reduce induced drag on fixed-wings,” in *2021 International Conference on Unmanned Aircraft Systems (ICUAS)*, Jun. 2021, pp. 1459–1465. doi: 10.1109/ICUAS51884.2021.9476801.

[16] S. Belferhat, S. M. A. Meftah, T. Yahiaoui, and B. Imine, “Aerodynamic optimization of a winglet design,” *EPJ Web of Conferences*, vol. 45, pp. 1–4, 2013.

[17] M. Prieto, M. S. Escarti-Guillem, and S. Hoyas, “Aerodynamic optimization of a VTOL drone using winglets,” *Results in Engineering*, vol. 17, no. 100855, 2023.

[18] J. Weierman, “Winglet design and optimization for UAVs,” M.S. thesis, Oklahoma State University, Stillwater, OK, USA, 2010.

[19] J. D. Anderson, *Fundamentals of Aerodynamics*, 6th ed. New York, NY, USA: McGraw-Hill Education, 2017.

[20] R. M. Cummings, S. A. Morton, W. H. Mason, and D. R. McDaniel, *Applied Computational Aerodynamics*. New York, NY, USA: Cambridge University Press, 2015.

[21] A. Schumacher, E. Sjögren, and T. Persson, “Winglet effect on induced drag for a Cessna 172 wing,” B.S. thesis, KTH Royal Institute of Technology, Stockholm, Sweden, 2014.

[22] xflr5, “Analysis of foils and wings operating at low Reynolds numbers.” Jan. 14, 2021. Available: https://www.xflr5.tech/xflr5.htm

[23] M. J. Queijo, “Theoretical span load distributions and rolling moments for sideslipping wings of arbitrary plan form in incompressible flow,” National Advisory Committee for Aeronautics, Langley, VA, USA, Rep. 1269, 1956.

[24] B. Maskew, “Program VSAERO theory document: A computer program for calculating nonlinear aerodynamic characteristics of arbitrary configurations,” National Aeronautics and Space Administration, Washington, D.C., USA, Rep. 4023, 1987.

[25] Flow5, “Flow solver, ‘An analysis tool for planes and sails operating at low Reynolds numbers.’” Accessed: Oct. 15, 2023. Available: https://flow5.tech/

[26] A. Deperrois, "F.A.Q: Why do I get the message 'Point is out of the flight envelope?'" xflr5. Available: https://www.xflr5.tech/docs/Point_Out_Of_Flight_Envelope.pdf

[27] G. Alfonsi, "Reynolds Averaged Navier Stokes Equations for turbulence modeling," *Applied Mechanics Reviews*, vol. 62, no. 040802, pp. 1–20, Jun. 2009.

[28] H. K. Versteeg and W. Malalasekera, *An Introduction to Computational Fluid Dynamics: The Finite Volume Method*, 2nd ed. London, UK: Pearson Education Limited, 2007.

[29] Ansys help, "4.1.5. The k-omega and SST Models." Accessed: Sep. 21, 2022. Available: https://ansyshelp.ansys.com/Views/Secured/corp/v221/en/cfx_mod/i1345900.html

[30] Ansys/CFX 2020 R1, "CFX-Solver Manager User's Guide." Ansys. Available: https://ansyshelp.ansys.com/account/secured?returnurl=/Views/Secured/corp/v221/en/cfx_solv/cfx_solv.html

[31] J. G. Leishman, *Introduction to Aerospace Flight Vehicles*. College Park, MD, USA: Embry-Riddle Aeronautical University, 2023.

[32] F. H. Norton, "An investigation on the effect of raked wing tips." National Advisory Committee for Aeronautics. Langley Field, VA, USA, NACA-TN-9, Nov. 01, 1921. Available: https://ntrs.nasa.gov/citations/19930080858

[33] C. A. Mahmood and R. K. Das, "Performance comparison of different winglets by CFD," *AIP Conference Proceedings*, vol. 2121, no. 1, p. 060006, Jul. 2019, doi: 10.1063/1.5115907.

[34] S. Gudmundsson, *General Aviation Aircraft Design: Applied Methods and Procedures*, 1st ed. Waltham, MA, USA: Butterworth-Heinemann, 2013.

[35] "Particle swarm optimization," *Wikipedia*. Oct. 26, 2023. Accessed: Nov. 12, 2023. Available: https://en.wikipedia.org/w/index.php?title=Particle_swarm_optimization&oldid=1181961286

[36] Flow5, "flow5 – Multi-objective particle swarm optimization." Accessed: Nov. 12, 2023. Available: https://flow5.tech/docs/flow5_doc/MOPSO/MOPSO.html

[37] M. D. Maughmer, T. S. Swan, and S. M. Willits, "Design and testing of a winglet airfoil for low-speed aircraft," *Journal of Aircraft*, vol. 39, no. 4, pp. 654–661, 2002, doi: 10.2514/2.2978.

[38] V. Madhanraj, K. G. Chandra, D. Swprazeeth, and B. D. Gopal, "Design and computational analysis of winglets," *Turkish Journal of Computer and Mathematics Education*, vol. 12, no. 7, pp. 1–9, 2021.

[39] P. Panagiotou, P. Kaparos, and K. Yakinthos, "Winglet design and optimization for a MALE UAV using CFD," *Aerospace Science and Technology*, vol. 39, pp. 190–205, Dec. 2014.

[40] K. Takenaka, K. Hatanaka, W. Yamazaki, and K. Nakahashi, "Multidisciplinary design exploration for a winglet," *Journal of Aircraft*, vol. 45, no. 5, pp. 1601–1611, Sep. 2008.

[41] J. Halpert, D. Prescott, T. Yechout, and M. Arndt, "Aerodynamic optimization and evaluation of KC-135R winglets, raked wingtips, and a wingspan extension," in *48th AIAA Aerospace Sciences Meeting Including the New Horizons Forum and Aerospace Exposition*, Jan. 2010. doi: 10.2514/6.2010-57.

[42] M. Heidari Soreshjani and A. Jahangirian, "An investigation on winglet design with limited computational cost, using an efficient optimization method," *Aerospace Science and Technology*, vol. 117, p. 106957, Oct. 2021.

[43] B. Makgantai, N. Subaschandar, and R. S. Jamisola, "A review on wingtip devices for reducing induced drag on fixed-wing drones," *Journal of Xi'an Univ. of Architecture & Technol.*, vol. XIII, no. 11, 2021, Accessed: May 18, 2023. Available: https://repository.biust.ac.bw/handle/123456789/403

INITIAL DISTRIBUTION LIST

1. Defense Technical Information Center
   Ft. Belvoir, Virginia

2. Dudley Knox Library
   Naval Postgraduate School
   Monterey, California